Experimental Aerodynamic Simulation of Glaze Ice Accretion on a Swept Wing

Andy P. Broeren and Mark G. Potapczuk NASA John Glenn Research Center, **Sam Lee** Vantage Partners Limited, **Brian S. Woodard** University of Illinois, **Michael B. Bragg** University of Washington, and **Timothy G. Smith** Federal Aviation Administration Technical Center

Abstract

Aerodynamic assessment of icing effects on swept wings is an important component of a larger effort to improve three-dimensional icing simulation capabilities. An understanding of ice-shape geometric fidelity and Reynolds and Mach number effects on iced-wing aerodynamics is needed to guide the development and validation of ice-accretion simulation tools. To this end, wind-tunnel testing was carried out for 8.9% and 13.3% scale semispan wing models based upon the Common Research Model airplane configuration. Various levels of geometric fidelity of an artificial ice shape representing a realistic glaze-ice accretion on a swept wing were investigated. The highest fidelity artificial ice shape reproduced all of the three-dimensional features associated with the glaze ice accretion. The lowest fidelity artificial ice shapes were simple, spanwise-varying horn ice geometries intended to represent the maximum ice thickness on the wing upper surface. The results presented in this paper show that changes in Reynolds and Mach number have only a small effect on the iced-wing aerodynamics relative to the clean-wing configuration. Furthermore, the addition of grit roughness to some lower-fidelity artificial ice shapes resulted in favorable lift and pitching moment comparisons to the wing with the highest fidelity artificial ice shape. For the wing with simple horn ice shapes, the dependence of maximum lift coefficient on horn height and angle are generally consistent with the trends observed for similar experiments conducted on iced airfoils in past research. In terms of usable lift however, the horn height did have a significant effect even for lower horn angles. This could be an important finding since usable lift may be more indicative of the impending iced-swept wing stall and need for additional pitch control than maximum lift coefficient.

I. Introduction

Ice accretion and the resulting aerodynamic effect on large-scale swept wings is an extremely complex problem that affects the design, certification and safe operation of transport airplanes. Broeren et al.[1] describe the current situation where there is increasing demand to balance trade-offs in aircraft efficiency, cost and noise that tend to compete directly with allowable performance degradations over a large range of icing conditions. These trade-offs, combined with the ever-present demand to reduce development cost, require an increased reliance on computational tool development. In addition, NASA is conducting research toward future generations of advanced airplane configurations with ambitious goals to improve efficiency while reducing emissions and noise. This research also relies on the development of advanced icing simulation tools in order to realize these design goals. However, sufficient high-quality data to evaluate the performance of these icing simulation tools on iced swept wings are not currently available in the public domain. This problem is being addressed through a large collaborative research effort sponsored by NASA, the Office National d'Etudes et Recherches Aérospatiales (ONERA) and the Federal Aviation Administration (FAA).

A main objective of this collaborative research effort was accomplished in the year 2016 with the publication of an experimental ice-accretion database for large-scale swept wings [2]. A primary purpose of this database is for the evaluation of three-dimensional icing simulation tools such as those being developed within NASA and ONERA [3,4]. There is an inherent difficulty as to how these comparisons should be conducted because of the large-scale, three-dimensionality associated with the experimental ice accretion in some cases (e.g., "scallops" or "lobster tails"). Furthermore, most icing simulations tools are not capable of predicting these large-scale, three-dimensional ice features. An important question is how much detail of this three-dimensional geometry is critical to the iced-wing aerodynamics and therefore must be accurately simulated. One possible comparison metric is the resulting potential aerodynamic degradation of the swept-wing. Therefore, the remaining objectives of the larger, collaborative research effort are to:

- Develop a systematic understanding of the aerodynamic effect of icing on swept wings including: Reynolds and Mach number effects, important flowfield physics and fundamental differences from 2-D.
- Determine the level of ice-shape geometric fidelity required for accurate aerodynamic simulation of swept-wing icing effects.

A series of papers published in 2018 provided initial results for these remaining objectives [5,6,7,8]. This paper, along with the companion works by Woordard et al.[9], Lee et al.[10] and Soltani et al.[11] continue to report these results. The approach used to accomplish these objectives has been successfully carried out in previous icing aerodynamics studies of straight wings and airfoils.

In past work, geometric representations of ice accretion have been attached to wings and models and tested in dry-air wind tunnels or in flight. These geometric representations are known as "artificial ice shapes" or "ice-accretion simulations." The various methods and geometric fidelities associated with developing artificial ice shapes has been investigated in a previous NASA-ONERA collaborative research effort called "SUNSET1" [12]. Since that time, a new

approach for producing high-fidelity artificial ice shapes has been developed using 3-D scanning and rapid-prototype manufacturing (RPM) [13,14]. In past studies of icing performance effects on airfoils, systematic investigations of Reynolds and Mach number effects were conducted [15,16,17,18,19,20,21]. Over the course of many years, it was found that aerodynamic tests conducted in the Reynolds number range of 1.0 to 2.0×10^6 could yield results applicable to flight Reynolds number (e.g., 10 to 20×10^6) for leading-edge ice shapes. Therefore, the current research effort will determine if similar trends apply for full-span, leading-edge ice on a swept wing. This effort involves both low- and high-Reynolds number aerodynamic testing. The low-Reynolds number aerodynamic testing is being conducted in the Wichita State University (WSU) 7-ft x10-ft size atmospheric wind tunnel. The high-Reynolds number aerodynamic testing is being conducted in the ONERA F1 11.4-ft x 14.8-ft pressurized wind tunnel using a larger scale model. The pressurization capability of this facility will allow for independent variations in Reynolds number up to approximately 12×10^6 and Mach number up to approximately 0.34. The results from the high-Reynolds number ONERA F1 test campaigns will be analyzed for Reynolds and Mach number effects (among other things) and compared to the results of the low-Reynolds number WSU test campaigns to determine the extent to which iced, swept-wing aerodynamic testing can be conducted in smaller-scale facilities at lower Reynolds number.

This paper focusses on the aerodynamic simulation fidelity of a swept-wing glaze ice accretion while the companion works [9,10,11] ocus on other ice accretions and comparison of results between the two wind-tunnel facilities. As shown later in Section II.C, the basic cross-sectional, ice-shape geometry is characterized by an upper-surface horn that is analogous to that often cited in studies of iced airfoils and straight wings. The aerodynamic simulation fidelity of horn ice on airfoils has been addressed in numerous past studies [12,19,22,23,24,25]. A key finding of this past work was that the aerodynamics of a glaze-horn ice shape could be replicated in experiments by replacing the entire ice-shape geometry with a simple shape (e.g., a rectangular spoiler) that mimicked the size and location of the upper and lower (if present) surface ice horns. Bragg et al.[19] provide a detailed explanation for the aerodynamics associated with this behavior. The flowfield of an airfoil with a horn-ice shape is dominated by the large separation bubble that forms downstream of the horn tip. The size of this separation bubble is governed essentially by the height and angle of the ice horn. Therefore, it is only necessary to replicate the height and angle with some lower fidelity geometry in order to produce a similar separation bubble and the resulting aerodynamic degradations. The remainder of the ice shape, not replicated by the simple geometry, has a relatively minor impact on the integrated aerodynamic performance, such as drag coefficient at low lift coefficient. Taking advantage of this finding, several researchers conducted parametric studies by systematically varying the horn height, angle, and type of airfoil section [26,27,28,29,30]. When the artificial ice horns were located at the airfoil leading edge and oriented directly into the oncoming flow, there was very little to no effect of changing the height of the ice over a reasonable range of values. Furthermore, the least aerodynamic impacts occurred at this location or locations on the lower surface of the leading edge. In contrast, as the artificial ice horn was located farther back on the upper surface side of the airfoil leading edge at larger angles to the oncoming flow, significant increases in aerodynamic degradations were observed. The trend of these effects was similar for differing airfoil designs as well, with only the relative magnitudes of the aerodynamic penalties being different.

The purpose of this present work is to investigate the effect of ice-shape geometric fidelity on aerodynamic performance for a glaze ice accretion on a swept wing, including simple geometric horn shapes. In order to carry out this objective, aerodynamic testing was conducted at the WSU wind tunnel and the ONERA F1 wind tunnel using 8.9% and 13.3% scale semispan wing models of the CRM65, respectively. The CRM65 geometry, described in Section II.B, is based upon the Common Research Model [1,31,32,33,34]. The high-fidelity artificial ice shape was based upon 3-D scans of a United States Code of Federal Regulations, Title 14, Part 25, Appendix C, Continuous Maximum (hereafter: App. C), glaze ice accretion in the NASA Icing Research Tunnel (IRT) and fabricated with rapid-prototype manufacturing. Additional artificial ice shapes were developed with decreasing geometric fidelity. The lowest-fidelity configurations were simple horn ice geometries that reproduced only the maximum upper surface ice thickness. The size and location of the simple horn geometry was parametrically varied to understand the associated tradeoffs. Aerodynamic performance testing was conducted in angle of attack sweeps over a Reynolds number range of 1.6×10^6 to 11.9×10^6 and a Mach number range of 0.09 to 0.34.

II. Wind-Tunnel Facilities, Models and Experimental Methods

A. Wind-Tunnel Facilities

The high-Reynolds number aerodynamic testing was carried out at the ONERA F1 pressurized wind tunnel located at the Fauga-Mauzac Center in southwestern France. The closed-return tunnel can be pressurized to 56 psi and has a test section approximately 11.5-ft high x 14.8-ft wide. The maximum speed is $M = 0.36$ at a pressure of approximately 22 psi which corresponds to a Reynolds number per foot of approximately 3.7×10^6. The maximum Reynolds number is 6.1×10^6/ft at a pressure of approximately 56 psi and $M = 0.23$. During an experiment, the Mach number was controlled to within ± 0.001 while the total pressure and total temperature were controlled to within ± 0.03 psi and ± 0.4 °F, respectively. The angle of attack sweeps were performed with a continuous change in pitch angle at a constant rate of 0.1 deg/sec. The model angle of attack was varied from -6 deg up to 25 deg, except in cases where dynamic forces limited the maximum angle of attack or a clear local maximum in lift coefficient was measured. Force balance and surface pressure measurements were acquired for most configurations at Reynolds and Mach number combinations shown in Table 1 along with the approximate values of total pressure (p_o) and dynamic pressure (q_∞). The speed control was based upon Mach number, therefore small differences in Reynolds number were observed. For example, the Reynolds number corresponding to $M = 0.23$ varied between 11.8×10^6 and 12.0×10^6. Torz-Dupuis [35] has provided a detailed report of the test set-up and instrumentation, data reduction, experimental uncertainties and wall corrections.

Load measurements were performed using a 6-component force balance located beneath the test section floor. This study utilized a reflection plane model and the force balance was used to measure the lift, drag and pitching moment. The force balance does not directly measure the lift and drag but rather it measures the normal force and the axial force which are relative to a coordinate system fixed to the force balance. A coordinate transformation is required to determine the lift and drag in the wind axes. The force balance measures the moment about a reference point fixed to the force balance and it is necessary to transfer the moment to the reference point on the model. For the 13.3% scale CRM65 model used in this test campaign there

was an offset along the *x*-axis of the force balance between the balance reference point and the model reference point. The model center of rotation and moment center are defined below in Section II.B. In general, the uncertainty of each force balance component was ±0.04% to 0.06% of the capacity. The measurement uncertainty in the wing angle of attack was ±0.023 deg. Specific uncertainty values for the wing forces and pitching moment are described later in this section.

Reynolds Number	Mach Number				
	0.09	0.18	0.23	0.27	0.34
1.6×10^6	$p_o = 18.9$ $q_\infty = 0.10$				
2.7×10^6		$p_o = 16.0$ $q_\infty = 0.35$			
4.0×10^6			$p_o = 18.9$ $q_\infty = 0.65$		
6.8×10^6		$p_o = 39.2$ $q_\infty = 0.88$	$p_o = 31.9$ $q_\infty = 1.1$	$p_o = 27.6$ $q_\infty = 1.3$	$p_o = 21.8$ $q_\infty = 1.7$
9.6×10^6		$p_o = 55.1$ $q_\infty = 1.2$			
11.9×10^6			$p_o = 55.1$ $q_\infty = 2.0$		

Surface pressure measurements were acquired using miniature electronic pressure scanning (ESP) modules developed by Pressure Systems. A total of six 64-channel ESP modules were used, each having a full-scale measurement range of ±15.0 psi. The pressure data acquisition system at F1 is designed to accommodate the changes in tunnel stagnation pressure for the various run conditions through changes in the reference pressure. The system ensures that the fullest range of the ESP modules is utilized without exceeding the measurement limit. Specific uncertainty values for model pressure coefficient are described later in this section. The wind-tunnel reference pressures are measured on individual Druck transducers. The resulting uncertainty in the dynamic pressure is an approximately linear function of the magnitude of the dynamic pressure and ranges from ±8.65% at the $Re = 1.6\times10^6$, $M = 0.09$ (lowest dynamic pressure) condition to ±0.46% at the $Re = 12.0\times10^6$, $M = 0.23$ (highest dynamic pressure) condition. This large range of uncertainty in dynamic pressure reflects the challenges of providing instrumentation for a pressurized wind tunnel where there is a correspondingly large range of pressures and forces to be measured.

The uncertainties in the experimental data were determined using the standard "root-sum-square" (RSS) method outlined by Coleman and Steele [36] and developed by Kline and McClintock [37]. These uncertainties are estimated for 20:1 odds and use the numerical values for the instrumentation described in the preceding paragraphs. Table 2 provides a summary of the absolute and relative uncertainties the model surface pressure coefficient for the lowest and highest dynamic pressure. The uncertainties for other Reynolds and Mach number conditions follows an approximately linear relationship with the corresponding dynamic pressure shown in Table 1. The data show that for pressure coefficients of about -5 or less, nearly all of the uncertainty is due to the dynamic pressure itself. For example,

the uncertainty in dynamic pressure for $Re = 1.6\times10^6$, $M = 0.09$ is ±8.65% while the uncertainty in the pressure coefficient is ±8.79% meaning 99% of the total uncertainty is due to the uncertainty in dynamic pressure. Table 3 provides a summary of the uncertainties in lift, drag and pitching moment coefficient for the lowest and highest dynamic pressure for the clean-wing configuration. For the lowest dynamic pressure at $Re = 1.6\times10^6$ and $M = 0.09$, the uncertainty values are large, especially for the drag and pitching-moment coefficients. The large uncertainties reported in Table 3 are due to low magnitude of the measured force and moment on the force balance. It is important to note that the force-balance uncertainties were reported based upon the maximum forces and moments for the current test. Therefore, the total uncertainties reported in Table 3 would likely be much smaller if the force-balance uncertainties were provided over the smaller range associated with the lowest dynamic pressure. In other words, the actual uncertainties in lift, drag and pitching-moment coefficient for the lowest dynamic pressure are likely much lower than the values reported in Table 3. Lee et al.[6] provide further justification for this conclusion by comparison of the data acquired on the 8.9% scale model at the WSU wind tunnel. For the highest dynamic pressure at $Re = 11.9\times10^6$, $M = 0.23$, all of the uncertainty values are much more reasonable and acceptable for the purposes of this work.

Test Condition	Pressure Coefficient	Absolute Uncertainty	Relative Uncertainty
$Re = 1.6\times10^6$, $M = 0.09$	±1	±0.116	±11.57%
	-5	±0.440	±8.79%
$Re = 11.9\times10^6$, $M = 0.23$	±1	±0.006	±0.62%
	-5	±0.023	±0.46%

Test Condition	Variable	Reference Value	Absolute Uncertainty	Relative Uncertainty
$Re = 1.6\times10^6$, $M = 0.09$	α	4.99 deg	±0.023 deg	±0.46%
	C_L	0.5607	±0.0530	±9.45%
	C_D	0.0203	±0.0115	±56.78%
	C_M	-0.2298	±0.0273	±11.86%
$Re = 11.9\times10^6$, $M = 0.23$	α	4.97 deg	±0.023 deg	±0.46%
	C_L	0.5951	±0.0038	±0.63%
	C_D	0.0186	±0.0007	±3.55%
	C_M	-0.2363	±0.0023	±0.96%

The force balance and surface pressure measurements were synchronized in time within the facility data acquisition system. This was important since the data were acquired as the model was pitched continuously at a rate of 0.1 deg/sec. A custom-designed, post-processing routine was written and implemented for these data to conditionally average the results into 0.5 deg angle of attack increments using a ±0.15 deg window based upon the geometric (uncorrected) angle of attack (α). For example, data acquired over the interval 3.85 deg ≤ α ≤ 4.15 deg were used to create conditionally averaged values for α = 4 deg. In addition to this, the pitching-moment coefficient referenced to quarter-chord of the mean aerodynamic chord was also calculated.

The low-Reynolds number aerodynamic testing was carried out in the Walter H. Beech Wind Tunnel at Wichita State University. The tunnel is an atmospheric, closed-return type, subsonic wind tunnel with a 7 ft x 10 ft test section. The maximum speed of the tunnel is approximately 350 ft/s which corresponds to a Reynolds number per foot of approximately 2.0×10^6/ft and a maximum dynamic pressure of 0.9 psi. The dynamic pressure was controlled to within ± 0.0007 psi over the entire operating range. The freestream turbulence intensity in the central region of the test section is approximately 0.07% of the freestream velocity. Force balance and surface pressure measurements were acquired at Reynolds numbers of 0.8×10^6, 1.6×10^6 and 2.4×10^6 which corresponded to freestream Mach numbers of 0.09, 0.18 and 0.27. The speed control was based upon Reynolds number, therefore small differences in Mach number were observed. For example, the Mach number corresponding to $Re = 1.6 \times 10^6$ varied between 0.17 and 0.18. The model angle of attack was varied from -6 deg to 25 deg. The specific angle of attack schedule was adjusted depending upon the model configuration.

Load measurements were performed using a 6-component pyramidal style force balance located beneath the test section floor. This study utilized a reflection plane model and the force balance was used to measure the lift, drag and pitching moment. For the 8.9% scale CRM65 model used in this test campaign there was an offset along the x-axis of the force balance between the balance reference point and the model reference point described below in Section II.B. In previous reports and papers [38,39,40], the pitching moment was referenced to this location. After conducting further analysis of the data, a determination was made to report the pitching moment about the quarter-chord of the mean aerodynamic chord location. The accuracy of the balance was 0.02% of full-scale. The uncertainty in the measured dynamic pressure was approximately ± 0.0007 psi.

Surface pressure measurements were acquired using pressure modules developed by Scanivalve. A digital sensor array (model DSA-3217) module with a range of ± 10.0 psi was used for pressure taps located near the leading edge of the model. Miniature pressure scanner (model MPS-4264) modules with ranges of ± 5.0 psi and ± 1.0 psi were used to measure the remaining surface pressures with an even distribution of pressure ranges as dictated by expected surface pressures. The accuracy, in percent of full-scale, was $\pm 0.05\%$, $\pm 0.06\%$, and $\pm 0.06\%$ for the 10 psi, 5 psi, and 1psi modules, respectively. This corresponds to an uncertainty of ± 0.005 psi, ± 0.003 psi, and ± 0.0006 psi, respectively, for the three ranges modules.

The uncertainties in the experimental data were determined using the standard methods described previously in this section for the F1 wind-tunnel data and more details of this analysis are reported in Ref. [40]. Table 4 provides a summary of the absolute and relative uncertainties in the wing angle of attack and performance coefficients calculated for an example point at $\alpha = 4$ deg with $Re = 2.4 \times 10^6$ and $M = 0.27$. All of these values were considered acceptable for this work.

Table 4. Absolute and Relative Uncertainties for WSU Wind-Tunnel Force Balance Data at $Re = 2.4 \times 10^6$ and $M = 0.27$.

Variable	Reference Value	Absolute Uncertainty	Relative Uncertainty
α	4.00 deg	± 0.05	$\pm 1.25\%$
C_L	0.5029	± 0.00137	$\pm 0.27\%$
C_D	0.0215	± 0.00068	$\pm 3.15\%$
C_M	-0.0067	± 0.0006	$\pm 9.01\%$

All aerodynamic data (α, C_L, C_M, C_D and C_P) presented in this paper were corrected for wind-tunnel-wall effects. The F1 wind-tunnel data were corrected using an in-house, linearized compressible flow method that models the potential flow around the model and wind-tunnel walls. The WSU wind-tunnel data were corrected using a procedure for 3D models outlined in Barlow et al.[41] as implemented by WSU [42]. The model and wind-tunnel constants used in this method were consistent between the WSU-related values to those of the F1 model and wind tunnel. The magnitude of the correction to the angle of attack applied to the WSU wind-tunnel data has been reduced relative to past papers and reports related to this project [38, 39, 40]. As described in Section I, aerodynamic data acquired at the WSU wind tunnel have been, and will be compared with data acquired at the ONERA F1 facility. Therefore, it is important that the effect of the wind-tunnel walls on the aerodynamic data from both facilities be accounted for properly. Lee et al.[6] provide comparison and analysis of the results of the wall correction schemes.

B. Wind-Tunnel Models Description

The two semispan wing models fabricated for these wind-tunnel tests were based on an 8.9% and 13.3% scale version of the CRM65 wing. The full-scale CRM65 geometry has a realistic cruise configuration loading applied to the wing resulting in a wing shear similar to dihedral [31]. In order to simplify the design of the removable leading edge segments (described below), this shearing or "bending" of the wing was removed from the model geometry resulting in an unsheared wing with a straight leading edge across the span of the model. The wing retains the twist and taper of the CRM65. Table 5 summarizes the geometric parameters of the semispan wing models, and a diagram of the 13.3%-scale CRM65 wing planform is shown in Fig. 1 with key dimensions. In the case of the 13.3% scale (F1 wind-tunnel) model, the main body was machined from stainless steel while the removable leading edge components were machined from aluminum. The model contained 243 pressure taps in its clean configuration. All components of the 8.9% scale (WSU wind-tunnel) model were machined from aluminum and contained 219 pressure taps in its clean configuration. Figure 2 shows photographs of the wing models installed in the respective wind tunnels with circular splitter plates. An artificial ice shape is mounted to the leading edge of the F1 wind-tunnel model while the WSU wind-tunnel model is shown in the clean configuration. Located below the circular splitter plate shown in the images, was a streamlined shroud that covered the wing spar. This arrangement isolated the wing spar from any aerodynamic loads. With this arrangement, both the splitter plate and shroud were non-metric meaning the aerodynamic forces were only measured on the wing itself. The splitter plate and shroud were designed based upon previous work for the smaller scale WSU wind-tunnel model [38,40].

Both models were designed and built with a removable leading edge that allowed artificial ice-shapes to be added to the wing. This approach has been used in previous icing aerodynamic studies [12,16,18,20,21] and allows for very efficient and repeatable changes in the artificial ice-shape configurations. This is important for this research effort, since many different ice-shape configurations were investigated. The main components of each model were: the main element (including a spar that attached to the force balance); a full-span clean leading edge; and a partial-span leading edge used for mounting ice shapes. An open channel exists between the main element and any of the leading edge components for routing pressure tubing out the base of the model to the data acquisition system. The seam between the clean leading edge and the main element was a

straight line on both the upper and lower surfaces, but the seam was not at the same location on both surfaces. The lower surface seam was sealed during testing to prevent any air leakage to the upper surface.

Table 5. Summary of 8.9% and 13.3% Scale CRM65 Semispan Wing Geometric Parameters.

Wing Parameter	13.3% Scale (F1 Model)	8.9% Scale (WSU Model)
Span, b	7.5 ft (90.00 in)	5.0 ft (60.00 in)
MAC	2.08 ft (25.01 in)	1.39 ft (16.67 in)
Area (Geometric)	13.55 ft^2 (1951.0 in^2)	6.01 ft^2 (865.3 in^2)
Volume	2.09 ft^3 (3604.5 in^3)	0.617 ft^3 (1069 in^3)
Aspect ratio†	8.3	8.3
Taper ratio	0.23	0.23
Root chord	3.38 ft (40.50 in)	2.25 ft (27.00 in)
Tip chord	0.77 ft (9.28 in)	0.52 ft (6.19 in)
Root α	4.4 deg.	4.4 deg.
Tip α	-3.8 deg.	-3.8 deg.
1/4-chord sweep angle	35 deg.	35 deg.
Leading edge sweep angle	37.2 deg.	37.2 deg.
Location of rotation center‡	$x = 29.05$ in., $z = 0$	$x = 19.37$ in., $z = 0$
Location of moment center‡	$x = 35.80$ in., $z = 0$	$x = 23.87$ in., $z = 0$
Location of 0.25×MAC‡	$x = 26.23$ in., $z = 0$	$x = 17.49$ in., $z = 0$

†--While the other parameters in this table are defined specifically for these models, the aspect ratio is defined for a complete airplane configuration using the formula, $\frac{(2 \; x \; semispan)^2}{2 \; x \; area \; of \; one \; wing}$.

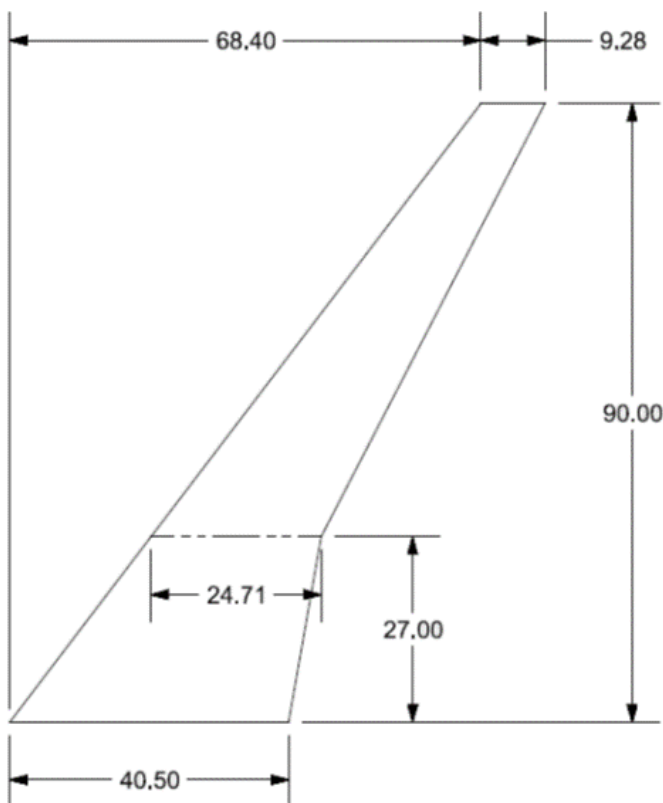‡--(0, 0, 0) is the wing root-section leading edge at zero angle of attack.

Figure 1. 13.3% scale CRM65 semispan wing planform with key dimensions labeled in inches.

Figure 2. Photographs of 13.3% scale CRM65 semispan wing installed in ONERA F1 wind-tunnel test section (top) and 8.9% scale CRM65 semispan wing installed in WSU wind-tunnel test section (bottom).

The partial-span removable leading edge was used to mount the artificial ice shapes to the wing. The partial-span removable leading edge extended from the root to 83.3% of the semispan for the 13.3% scale model and from the root to 50% of the semispan for the 8.9% scale model. Both contained a portion of the airfoil contour on the lower surface. Artificial ice shapes were attached to these removable leading edges and covered the entire wing upper surface. Outboard of this partial-span leading edge, the artificial ice shapes were attached directly to the main element. The reason for this is that the

model thickness decreases significantly on the outboard portion of the wing and there was not enough material to extend the removable leading edge. This design does not adversely affect the efficiency or repeatability of the artificial ice-shape configuration changes.

The artificial ice shapes were created using a rapid prototype manufacturing (RPM) technique called stereo-lithography (SLA). The SLA process utilizes an ultraviolet laser to solidify liquid polymer resins. The majority of the artificial ice shapes were manufactured from the Somos NeXt brand polymer while some of the initial ice shapes were rapid prototyped using a different polymer called Accura 60. Tolerances are advertised to be about +/- 0.005 inches for this process. A representative ice shape was added to the necessary wing geometry for each segment of wing span. The leading edge was divided into three segments for the 13.3% scale model and two segments for the 8.9% scale model. All segments were approximately 37.5 in long. Pressure taps were installed in each of these segments at the same locations as on the clean removable leading edge. The pressure tap holes were included in the RPM design, and then stainless steel tubes were glued into each hole and plumbed to the quick disconnect located inside the channel between the removable leading edge and the main element.

The pressure taps in the models were distributed in streamwise-running rows across the span of the models. The 8.9% scale model also had upper-surface pressure taps located in four rows oriented perpendicular to the wing leading edge. Details regarding the pressure tap locations can be found in Ref. [5] for the 13.3% scale model and in Refs. [38,40] for the 8.9% scale model.

C. Artificial Ice-Shape Configurations

In addition to the clean aluminum machined leading edge, several other leading-edge configurations were tested. Numerous artificial ice shapes have been developed for aerodynamic testing and are summarized by Camello et al.[39] for the 8.9% scale CRM65 wing tested at WSU. Selected configurations were also tested at F1 on the 13.3% scale model [5,6,7]. This paper provides a more detailed study, along with new data, for artificial ice shapes based upon a single ice accretion referred to as "WB33." Ice accretion testing was performed in the NASA IRT on three individual sections of the full-scale CRM65 reference wing: one taken at $y/b = 0.20$ called the Inboard model; one taken at $y/b = 0.64$ called the Midspan model; and one taken at $y/b = 0.83$ called the Outboard model [2]. As shown in Table 6, the WB33 icing conditions were scaled from App. C to the airspeed of 130 knots and the near sea-level altitude of the IRT and represent a holding condition for the CRM65 airplane in Continuous Maximum icing. Photographs of the resulting ice accretion on each of the three models are shown in Fig. 3. The relatively warm total air temperature and high cloud liquid water content resulted in the glaze ice accretion with very large roughness features yet no discernable, or repeated pattern (such as traditional scallops or lobster tails). The ice geometry was measured using the 3D laser scanning method [13] and the scan data were used to determine the maximum combined cross section (MCCS) of the ice accretion. The MCCS [2] was derived from 30 section cuts over a six-inch spanwise segment of the 3D ice scan. The section cuts were projected onto a single plane and the maximum outer boundary was obtained. The resulting MCCS profile represents the outermost extent of the ice shape over that six-inch segment. Figure 4 presents the MCCS profiles for the ice accretion shown in Fig. 3. These cross sections exhibit the classic characteristics of glaze ice with the distinctive upper-surface horn geometry.

10/19/2016

Table 6. Summary of Icing Conditions for "WB33" Ice Accretion.

Icing Conditions	Flight Reference	IRT Scaled
Altitude (ft)	10,000	1,278
Angle of Attack (deg)	3.7	3.7
Speed (kts)	232	130
Total Temperature (°C)	1.1	-3.1
Static Temperature (°C)	-6.0	-5.3
Cloud MVD (μm)	20	27
Cloud LWC (g/m^3)	0.51	0.91
Exposure Time (min)	45	45

Figure 3. Photographs of WB33 ice accretion on Inboard (top), Midspan (middle) and Outboard (bottom) models.
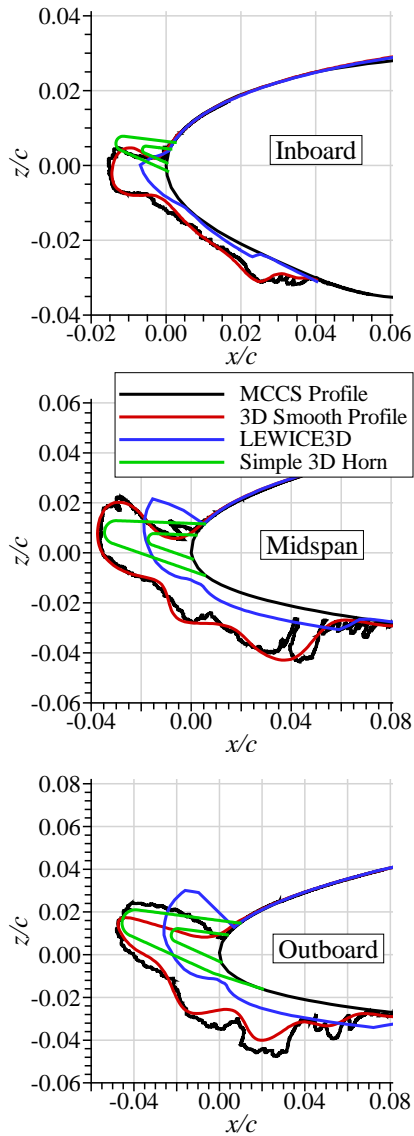
Figure 4. Comparison of the various ice-shape profiles for each of the three IRT models with the simple 3D horn.
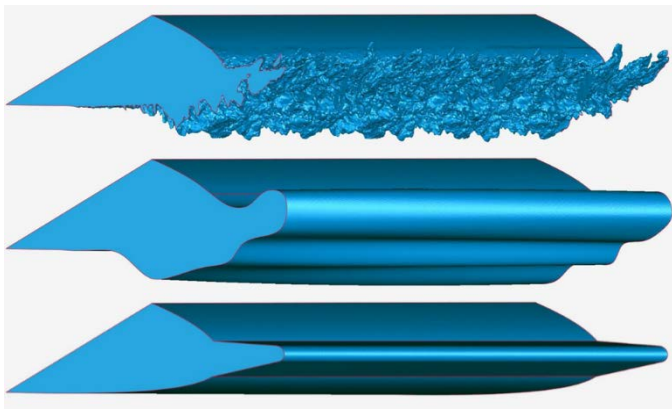

Figure 5. Comparison of WB33 high-fidelity artificial ice shape geometry (top) with the lower-fidelity, 3D smooth geometry (middle) and simple 3D horn ice shape (bottom).

The 3D scan data from this case were used to create full-span artificial ice shapes for aerodynamic testing. Camello et al.[43] describe the process used to create the full-span, high-fidelity artificial ice shapes. In this case, "high-fidelity" means that the artificial ice shapes contained nearly all of the three-dimensional features depicted in Fig. 3. Camello et al.[43] also describe the methodology used to create lower-fidelity versions of these ice shapes. A "3D smooth" ice shape was also created from the high-fidelity geometry by taking various section cuts along the span, smoothing these cuts and then lofting them into a solid geometry. The 3D smooth ice shape varies along the span of the wing, but does not contain any scallop type features, feathers or other ice roughness. A qualitative comparison of the high-fidelity and 3D-smooth geometries is shown in Fig. 5. The 3D smooth ice shape is clearly much smoother and more solid than the high-fidelity ice shape. A quantitative comparison of the cross sections is shown in Fig. 4 where the level of ice-shape smoothing can also be seen. The 3D smooth profiles do represent the typical outer profiles of the ice accretion.

Another lower-fidelity version of the WB33 ice shapes was developed based upon a LEWICE3D simulation for the CRM65 airplane operating in the holding conditions given previously in Table 6 (flight reference case). Yadlin et al. [44] describe the computational approach whereby a 3D RANS simulation of the CRM65 wing-body airplane configuration was performed using OVERFLOW at the appropriate flight conditions. The flow solution was then used as input for the LEWICE3D simulation that was performed using a 7-bin drop size distribution and the ice density set to 450 kg/m^3. This analysis used the Boeing version of LEWICE3D incorporating various best practices within the Boeing Company. A total of 48 ice shape profiles were generated along the span of the CRM65 wing. These cuts were then lofted into a solid ice shape used to manufacture the corresponding artificial ice shape aerodynamic testing. A comparison of the profiles is also depicted in Fig. 4. While the LEWICE3D generated ice shape generally has the same shape as the MCCS profile, it is clearly smaller in size, particularly for the upper-surface horn thickness. For the Midspan and Outboard model comparisons, the LEWICE3D upper surface horn is located farther back on the upper surface meaning that it makes a larger angle relative to the oncoming flow.

The comparison of the LEWICE3D and IRT MCCS results shown in Fig. 4 led to a major focus of this paper on the effects of simple 3D horn ice. The objective is to understand the tradeoff between upper surface horn height and horn angle. Similar studies have been conducted for iced airfoils [26,27,28,29,30] as discussed in Section I. A series of simple 3D horn ice geometries were developed and resulted in additional artificial ice-shape configurations for this investigation. The geometry of simple 3D horn ice is illustrated by the cross-sections shown in Fig. 4 and the 3D rendering in Fig. 5. Figure 4 shows both the baseline height and a smaller horn cross-section that was exactly one-half of the baseline horn height. As can be seen in Fig. 4, the normalized horn height and the horn angle with respect to the local chord line vary along the span. This variation was partly based upon the variation observed in the 3D smooth profile, although the agreement is not exact as indicated in Fig. 4. It is important to note that the simple 3D horn ice was not intended to exactly replicate the aerodynamics of the WB33 ice shape. However, the WB33 ice geometry was used to define a representative simple 3D horn geometry with appropriate spanwise variation. In addition to the two horn heights that were tested, the horn angle (and thus its location) was also systematically varied. The range of horn angles/locations is depicted in Fig. 6. The horn geometries were

oriented perpendicular to the local surface tangent and the horn angle was defined relative to the chordline. Since the normalized horn height and angle vary along the span of the wing, reference values are given here for the Midspan IRT model station (middle plots of Figs. 4 and 6). There were two different horn height values of $k/c = 0.0177$ and 0.0355. There were three different horn angles of $\theta = 10$, 25 and 40 deg. The different horn angles were applied uniformly along the span of the wing. As shown in Fig. 6, this range of heights and angles approximately captures the variation overserved between the 3D smooth profile and the LEWICE3D ice shape.
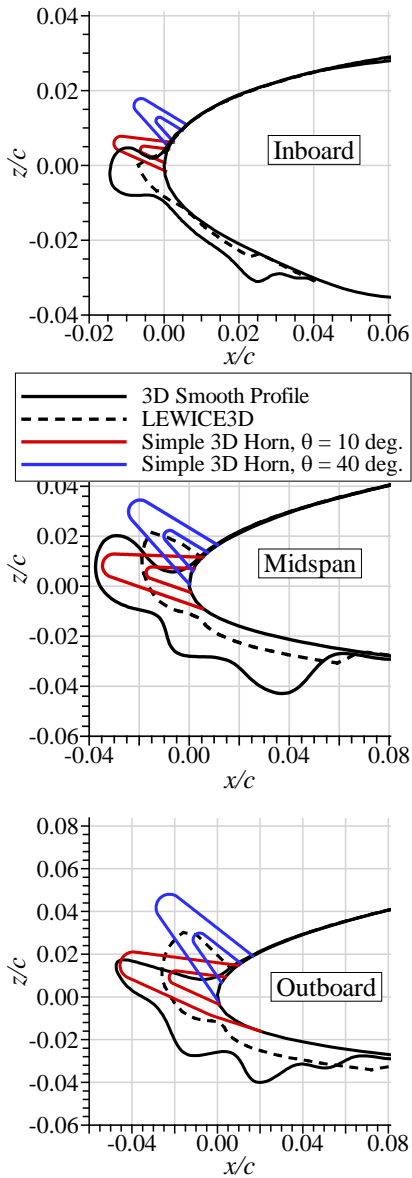
Figure 6. Comparison of the 3D Smooth and LEWICE3D ice-shape profiles with the simple 3D horn ice shape profiles with $k/c = 0.0355$ and 0.0177 as defined on the Midspan Model.

In most cases, the lower-fidelity artificial ice shapes were tested in both the smooth condition and with grit roughness applied to the surface. The grit size was based upon the guidance in FAA Advisory Circular 25-25A that suggests a height of 3 mm on the full-scale reference airplane. The grit was applied to the surface of the smooth ice shape with "full coverage" meaning that all of the surface was

covered with the silicon carbide grains. The equivalent roughness size for the 13.3% scale model was 46 grit and for the 8.9% scale model it was 60 grit. The grains were adhered to the surface of the artificial ice shape with two-part epoxy.

III. Results and Discussion

The aerodynamic results presented here are organized as follows. The effect of geometric fidelity for the WB33 ice accretions is discussed first along with the review of certain performance parameters previously introduced by Broeren et al. [5]. The results of the simple 3D horn ice are presented including the effects of: Reynolds and Mach number; and horn height and location. Finally, a summary of simple 3D horn ice shape effects is discussed.

A. Effect of WB33 Artificial Ice Shapes on Wing Performance

As described in Section II.C, there were two lower-fidelity representations of the WB33 glaze ice accretion created for this investigation. The aerodynamic performance effect of these ice shapes on the CRM65 wing is summarized in Fig. 7 for the 8.9% scale model in the WSU wind tunnel a Reynolds number of 2.4×10^6 and $M = 0.26$. These results clearly show that the lower-fidelity geometries resulted in less conservative degradations to the clean wing lift and drag coefficients relative to the high-fidelity geometry that maintained all of the three-dimensional features of the original ice accretion. Interestingly, the 3D smooth and LEWICE3D artificial ice shapes resulted in similar aerodynamic performance despite the differences in the cross-section geometries shown in Fig. 4. The most significant difference between these two configurations was in drag coefficient for low lift coefficient less than about 0.4. The effect of adding the 60-grit size roughness to the smooth artificial ice shapes is shown in Fig. 8. Looking at the lift and pitching moment coefficient data, it can be seen that the addition of roughness significantly improves the comparison with the high-fidelity artificial ice-shape configuration. In the case of drag coefficient, there is some improvement in the comparison, but significant differences between the high-fidelity and lower-fidelity configurations remain.

The effect of the $k/c = 0.0355$ simple 3D horn ice on the wing aerodynamic performance is shown in Fig. 9. The lift and pitching moment data for the lower horn angle ($\theta = 10$ deg) case compare closely to the 3D smooth and LEWICE3D configurations despite the significant differences in geometry described in Section II.C. The geometric differences were made manifest in drag coefficient for low lift coefficient less than about 0.2. The tradeoff between the simple 3D horn height and angle is depicted in Fig. 10. Careful inspection of the lift coefficient shows that increasing the horn angle from 10 to 25 deg had a larger impact than increasing the horn height from $k/c = 0.0177$ to 0.0355. However, the pitching moment behavior in the region of the minimum C_M, was significantly affected by changes in both the horn height and angle. As discussed in the following section, such changes are indicative of the stall progression on the wing. The results in drag coefficient were also mixed. Changes in horn height had minimal effect compared to changes in horn angle at minimum drag. However, both the horn height and angle contributed to changes in drag for lift coefficients greater than about 0.2.
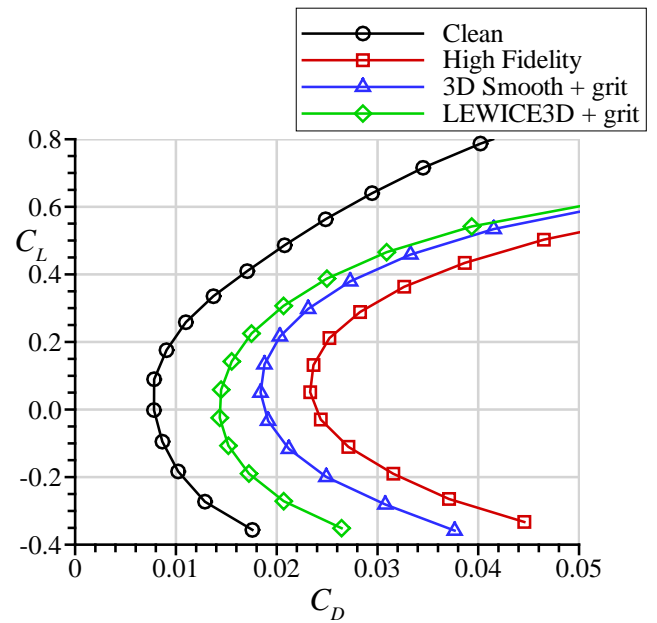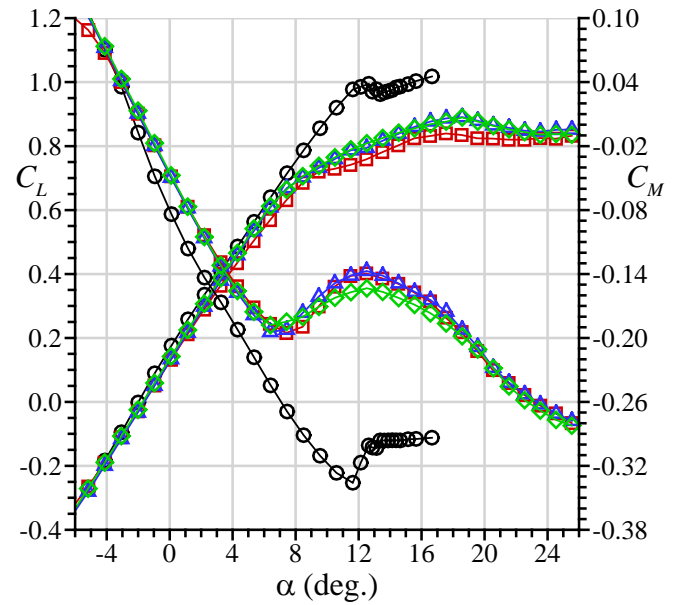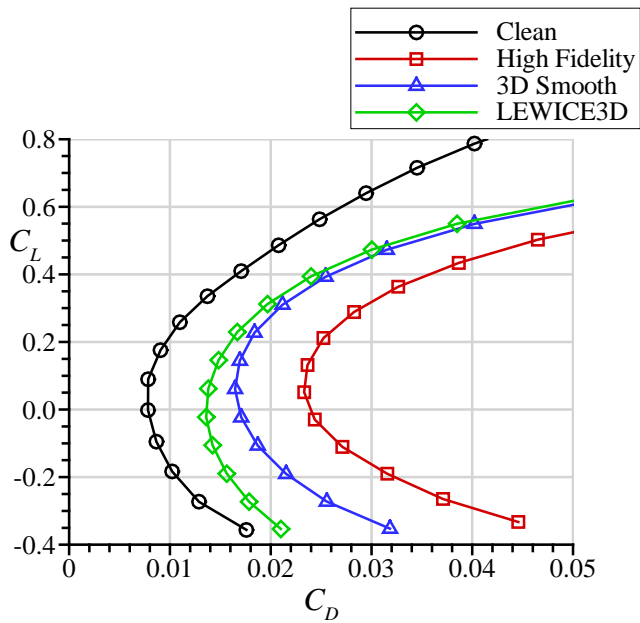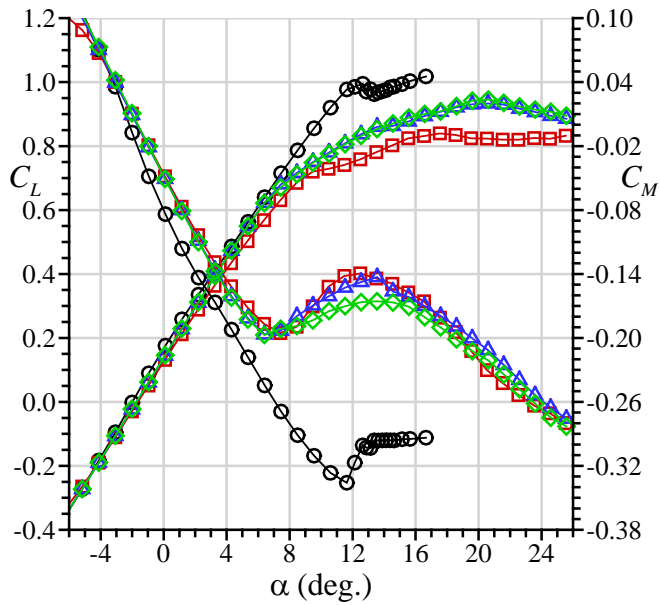
Figure 7. Comparison of iced-wing performance effects for various levels of geometric fidelity of the WB33 ice accretion from the WSU wind tunnel at $Re = 2.4 \times 10^6$ and $M = 0.26$.

Figure 8. Comparison of iced-wing performance effects with grit roughness added to the lower-fidelity artificial ice shapes of the WB33 ice accretion from the WSU wind tunnel at $Re = 2.4 \times 10^6$ and $M = 0.26$.
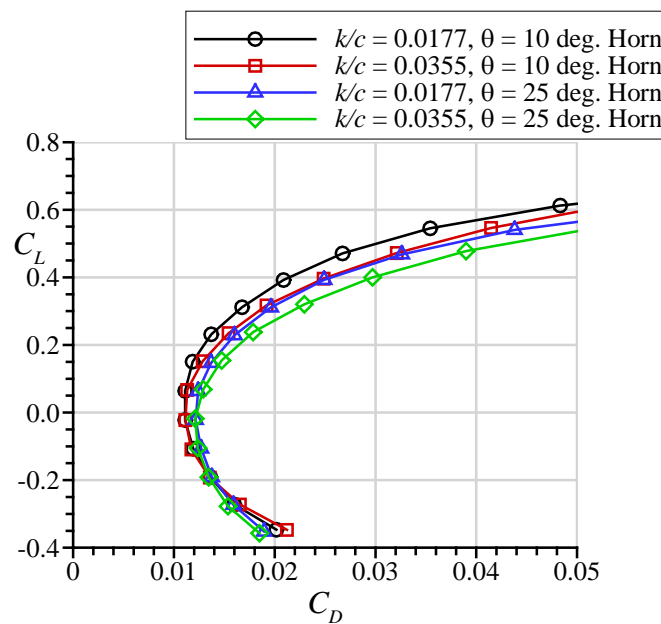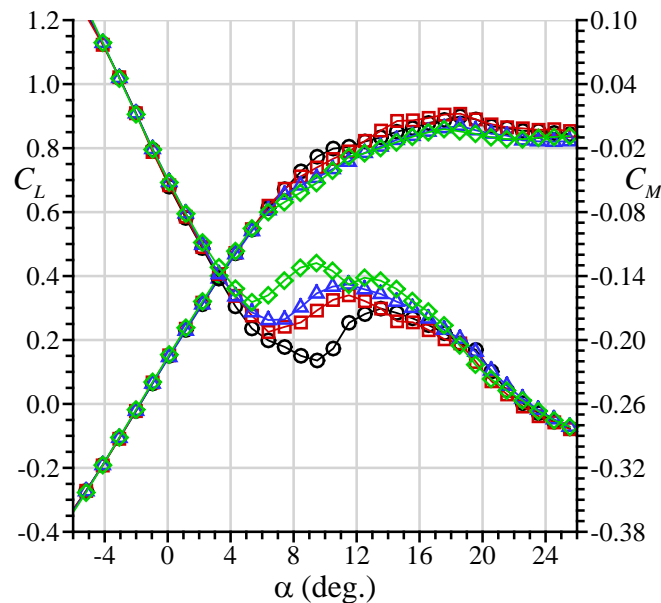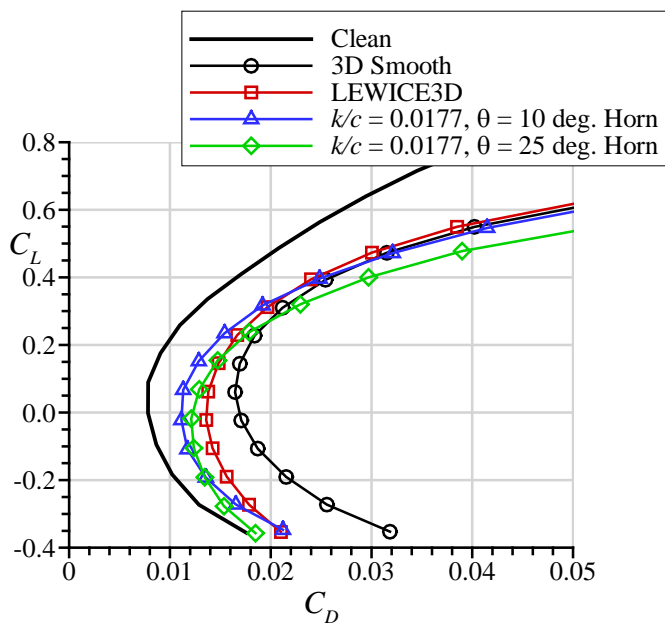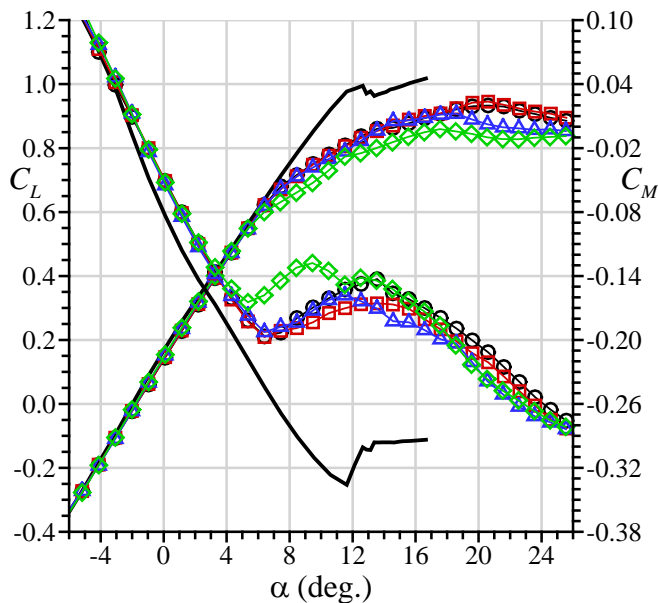
10/19/2016

Figure 9. Comparison of iced-wing performance effects including the simple 3D horn ice shapes from the WSU wind tunnel at $Re = 2.4 \times 10^6$ and $M = 0.26$.

Figure 10. Comparison of iced-wing performance showing the tradeoff between simple 3D horn ice shape height and angle from the WSU wind tunnel at $Re = 2.4 \times 10^6$ and $M = 0.26$.

The lift curves shown in Figs. 7-10 for the wing with artificial ice shapes were characterized by some common features relative to the clean-wing configuration. These lift-curve characteristics were related to changes in the pitching moment that is also plotted against angle of attack for direct comparison. For the iced-wing configurations, the lift-curve slope begins to decrease significantly in the same angle of attack range where the pitching moment reaches the first local minimum. For example, consider the high-fidelity configuration (cf. Fig. 7) for angles of attack between 6 and 8 deg where C_M approaches a local minimum and the lift curve indicates a significant departure from the clean configuration. The data show that C_L continues to increase for the iced-wing configurations up to relatively high angles of attack. These characteristics associated with the iced-wing lift curves in the stall regions prompted analysis designed to clearly identify a set of performance parameters used to

summarize the large data set from this research effort. This analysis is described in the next section.

B. Definition of Aerodynamic Performance Parameters

1. Lift-based Parameters

Iced aerodynamics has traditionally focused on maximum lift coefficient and the corresponding angle of attack as the most significant and easily identifiable performance parameters. Maximum lift coefficient is defined as the first local maximum in the lift curve with the corresponding angle of attack designated as the stall angle. Using the clean configuration as an example, $C_{L,max} = 0.99$ at $\alpha_{stall} = 12.6$ deg (cf. Fig. 7). For the iced-wing configurations shown in Figs. 7-10, the maximum lift coefficients are fairly well defined by a local maximum. However, these $C_{L,max}$ values are associated with stall angles that are larger than for the clean wing. The iced-wing configurations shown in Fig. 7 have stall angles ranging from 17.5 to 20.6 deg. In other cases, the corresponding stall angles were also higher than the clean-wing value, as high as $\alpha_{stall} = 22.7$ deg. This represents a fundamental difference from past research on straight wings or airfoils with large, leading-edge artificial ice shapes where the stall angle was lower the clean-wing value. The lift curves for some configurations acquired at different Reynolds and Mach number conditions exhibited poorly defined local maxima where there was more of a "plateau" in the lift curve instead of a well-defined "peak." Therefore the use of maximum lift coefficient and stalling angle may not necessarily be indicative of the stall progression on the CRM65 swept wing with artificial ice shapes. The large reduction of lift-curve slope shown for the iced-wing configurations in Figs. 7-10 indicates significant flow separation. This separation occurs on the outboard portions of the wing that is represented in Figs. 7-10 by the changes in the pitching-moment curve. The outboard flow separation has also been determined through analysis of the flow visualization and surface-pressure distributions [5,38].

In 1957, Furlong and McHugh published a National Advisory Committee for Aeronautics (NACA) technical report summarizing the low-speed aerodynamic characteristics of swept wings based upon all known data collected through August 15, 1951 [45]. Furlong and McHugh identified a performance-based parameter called "usable" lift or "inflection" lift based upon their review of previous work. For convenience, the authors assumed that the quarter-chord *MAC* location was coincident with the airplane center of gravity. Therefore, the longitudinal stability could be referred to as either stable or unstable depending upon the slope of the pitching-moment curve with respect to angle of attack. The change from a negative slope to a positive slope thus indicated a change from a longitudinally stable to unstable situation. The term inflection lift refers to the inflection point, or local minimum, in the C_M vs α curve representing the change in slope. The authors also clarified that the term usable lift coefficient represents the lift coefficient beyond which stall control is required. This interpretation of usable lift implies that a certain amount of flow separation on the wing has crossed some threshold such that this value of the usable lift coefficient may be more significant than the absolute value of the maximum lift coefficient. This interpretation of usable lift is applicable to the iced-wing aerodynamic effects observed within the present data set. The high-fidelity configuration can be used as an example to illustrate the interpretation of usable lift coefficient as a meaningful performance metric. As shown in Fig. 7, the first local minimum in C_M ($C_{M,min} = -0.20$) occurred at $\alpha_{use} = 7.4$ deg and $C_{L,use} = 0.63$. Thus, the identified usable lift coefficient provides an

indication of the lift coefficient that can be attained in this configuration before significant flow separation develops over the wing that could require additional pitch control.

Broeren et al. [5] demonstrated how the concept of usable lift can be employed to describe where the wing begins to stall in a way that is consistent with the original definition proposed by Furlong and McHugh [45]. It is important to note that the inflection point, or first local minimum, in the pitching moment that identifies $C_{L,use}$ is not always well defined. There are some cases where the C_M curve tends to flatten out in the region of the first local minimum and can sometimes be followed by a second minimum. Usually for such configurations, there was not as significant of a change in the stall progression over these angles of attack. This type of ambiguity in the usable lift coefficient is analogous to the situation in defining the maximum lift coefficient where the lift curve tends to reach a plateau rather than having a well-defined local maximum. Therefore, the information provided by both $C_{L,use}$ and $C_{L,max}$ can be taken together as complementary performance-based parameters.

2. Drag-based Parameters

The artificial ice-shape configurations developed for aerodynamic testing were partly based upon typical airplane holding scenarios in App. C conditions. As a result, the leading-edge ice shapes were large as in the WB33 ice accretion shown in Section II.C. In 2001, Lynch and Khodadoust published, "a systematic and comprehensive review, correlation, and assessment of test results available in the public domain which address the aerodynamic performance and control degradations caused by various types of ice accretions on the lifting surfaces of fixed wing aircraft" [46]. The authors directly address the importance of drag penalties due to leading-edge ice accretion stating that such penalties are a concern because they can lead to reductions in aircraft climb and acceleration gradients, range and speed. They point out that accidents and incidents have been reported with autopilots not augmented with autothrottle during icing exposure where the airspeed can be reduced to stall entry without warning. In addition to these practical considerations, it is important from a research perspective to understand how the drag coefficient may be affected by changes in ice-shape fidelity and Reynolds and Mach number.

Lynch and Khodadoust [46] suggested two conditions for the assessment of icing-related drag penalties. The first condition is simply the value of the minimum drag coefficient. For the clean and iced-wing configurations in this paper, the minimum drag coefficient is always near zero lift because of the influence of induced drag for non-zero lift coefficients. The other condition that Lynch and Khodadoust recommend is that corresponding to a flight speed 30% above the 1-g stall speed ($V_{s,1g}$) for the clean reference geometry. This is equivalent to a lift coefficient that is 59% of $C_{L,max}$ for the clean wing. As reported by Broeren et al.[5], there is a significant dependence of the clean wing $C_{L,max}$ upon Reynolds and Mach number, with values ranging from 0.98 to 1.23. In order to simplify the analysis of iced-wing drag penalties, a reference value of $C_L = 0.6$ was selected which corresponds to a $C_{L,max} = 1.014$ for a speed of $1.3 V_{s,1g}$. The reference value of $C_L = 0.6$ was also selected because it is lower than all of the values of $C_{L,use}$ identified for the iced-wing configurations of Broeren et al. [5]. This means that the drag penalties associated with this lift coefficient are still within the range of lift coefficient prior to the onset of significant stall progression on the wing. All of the drag-polar data were analyzed to determine the minimum drag coefficient and the drag coefficient at $C_L = 0.6$.

C. Clean and Iced Wing Reynolds and Mach Number Effects

The pressurization capability of the F1 wind-tunnel was exploited in order to determine the Reynolds and Mach number effects on the aerodynamic performance of the clean and iced wing. As illustrated in Table 1, performance data were acquired over a range of Reynolds numbers at constant Mach numbers of 0.18 and 0.23 while performance data were acquired over a range of Mach numbers at a constant Reynolds number of 6.8×10^6. An even larger matrix of run conditions was used in a previous F1 wind-tunnel test campaign described by Broeren et al.[5] for the clean wing and certain iced-wing configurations. The authors also described in detail the independent effects of Reynolds and Mach number. For the purposes of this paper, the performance parameters described in the previous section are plotted against Reynolds number for all Mach numbers. For example, Fig. 11 summarizes the effect of WB33 artificial ice shapes on $C_{L,max}$ and $C_{L,use}$. The large variation in the clean wing lift coefficients at a fixed Reynolds number is caused by differences in Mach number. As described by Broeren et al.[5], the lift coefficients increase with increasing Reynolds number, but they decrease with increasing Mach number. In contrast for the iced-wing configurations, the lift coefficients show very little dependence upon Reynolds or Mach number over the range tested. The largest differences tend to be for the data acquired at the lowest Mach number of 0.09. The effect of artificial ice shape fidelity upon $C_{L,max}$ is consistent with the data from the WSU wind tunnel shown in Fig. 8 where the lower-fidelity simulations resulted in higher $C_{L,max}$ relative to the 3D high-fidelity configuration. In terms of usable lift, the results in Fig. 11 show that the LEWICE3D + grit configuration had a lower value of $C_{L,use}$ than for the 3D high fidelity configuration. This is also consistent with the data from the WSU wind-tunnel shown in Fig. 8 where it can be seen that $C_{M,min}$ occurred at the lower angle of attack and thus lower lift coefficient for the LEWICE3D + grit configuration relative to the 3D high-fidelity configuration.

The effect of Reynolds and Mach number variation on the drag-based performance parameters is shown in Fig. 12 for the same configurations as in Fig. 11. The data show that there is little to no effect of Mach number on the selected drag coefficients. For the iced-wing configurations, the drag coefficients tend to decrease, in a nearly linear trend, with increasing Reynolds number over the range tested. Furthermore, the data in Fig. 12 are consistent with Fig. 8 where the 3D high fidelity configuration had the largest drag coefficient values.

The effect of Reynolds and Mach number variation on the lift-based performance parameters is shown in Fig. 13 for the simple 3D horn ice shapes. In general, the results are similar to the iced-wing configurations shown previously in Fig. 11. However, there does appear to be more significant Mach number effects for the $k/c = 0.0355$, $\theta = 10$ deg horn both with and without grit roughness. This is particularly clear in the plot of usable lift at a fixed Reynolds number of 6.8×10^6 where the Mach number varies from 0.18 to 0.34. In addition, the $k/c = 0.0355$, $\theta = 10$ deg horn (without grit roughness) exhibited more variation in $C_{L,max}$ from $Re = 1.6 \times 10^6$ to 4.0×10^6, than the previous iced-wing configurations from Fig. 11. The data show that the addition of grit roughness had some effect on the lift-based parameters for the $k/c = 0.0355$, $\theta = 10$ deg horn, particularly for $Re \leq 4.0 \times 10^6$. For the larger horn angle, $\theta = 40$ deg, less dependence of both $C_{L,max}$ and $C_{L,use}$ on Reynolds and Mach number was observed with grit roughness added to the simple 3D horn geometries.

The effect of Reynolds and Mach number variation on the drag-based parameters is shown in Fig. 14 for the same configurations as Fig. 13. The results for minimum drag coefficient are similar to that previously discussed in connection with Fig. 12 where there is little to no effect of Mach number. An exception to this observation exists for the $k/c = 0.0355$ horn at $\theta = 40$ deg + grit configuration, where there was more variation in both $C_{D,min}$ and $C_{D,0.6}$ over the different Mach numbers. This is readily seen for the fixed $Re = 6.8 \times 10^6$ where the Mach number varies from 0.18 to 0.34. Also consistent with Fig. 12 is the trend of nearly linear decreases in $C_{D,min}$ with increasing Reynolds number over this range. On the other hand, there were more significant differences in the plot of drag coefficient at the lift coefficient of 0.6. For both $k/c = 0.0177$ and 0.0355 horns at $\theta = 40$ deg (with grit roughness), $C_{D,0.6}$ was significantly lower at $Re = 1.6 \times 10^6$ than for $Re \geq 2.7 \times 10^6$. At this time, the reason for this behavior is unclear. However, it should be noted that the values of $C_{L,use}$ for these configurations were less than 0.6. This implies that the iced wing has begun to stall at the lift coefficient of 0.6 where this C_D value was determined. This fact may play a role in the Reynolds number variation of $C_{D,0.6}$ for these configurations. Taken together, both drag-based parameters show an increase due to the addition of grit roughness on the $k/c = 0.0355$ horn at $\theta = 10$ deg. Even larger increased in drag were observed when the horn angle was increased to $\theta = 40$ deg.

In general, the aerodynamic performance data acquired on the wing with artificial ice shapes exhibited little variation with changes in Reynolds and Mach number over the range tested when compared against the clean-wing configuration. This variation was the least for the various WB33 artificial ice shapes such as the 3D high-fidelity, 3D smooth + grit and LEWICE3D + grit configurations. The aerodynamic data for the wing with the simple 3D horn ice configurations did exhibit slightly more variation with Reynolds and Mach number, but still significantly less than the clean configuration.
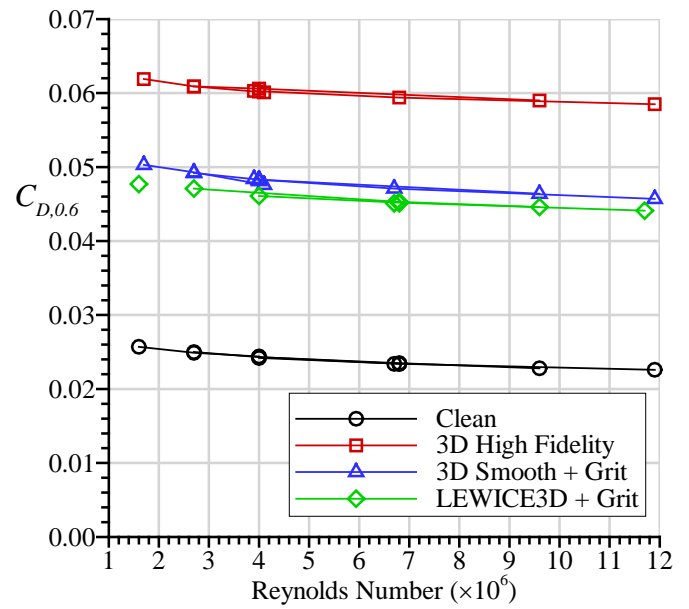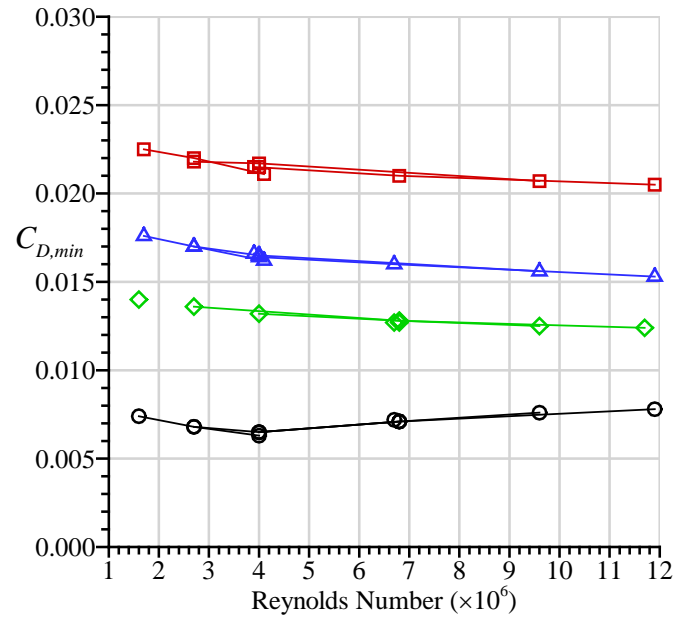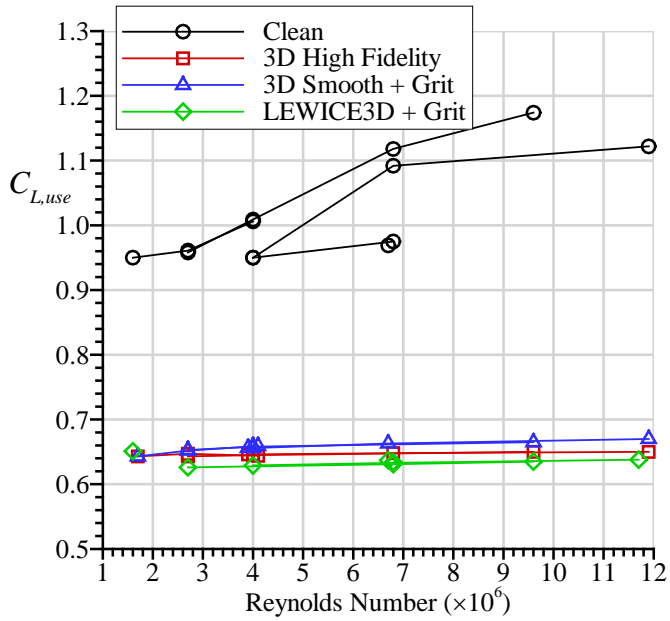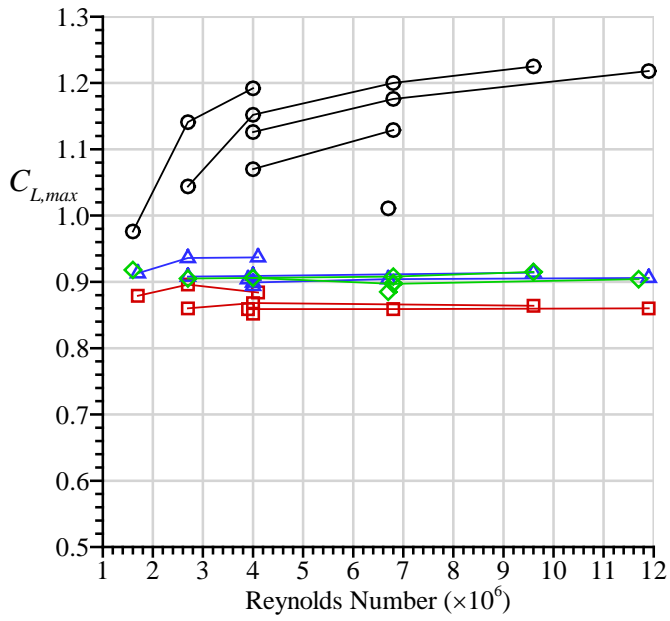
10/19/2016

Figure 11. Effect of Reynolds number on maximum and usable lift coefficients for clean and iced wing with WB33 artificial ice shapes having various levels of geometric fidelity from the F1 wind tunnel at $M = 0.09$ to 0.34.
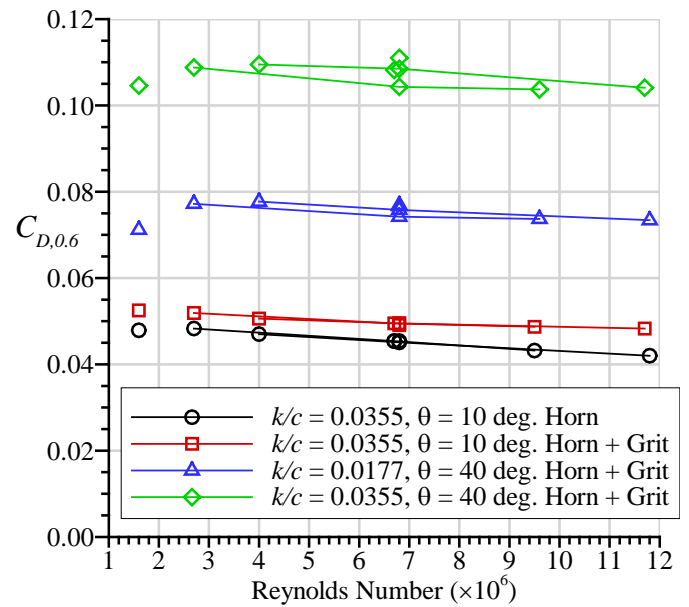
Figure 12. Effect of Reynolds number on minimum and $C_L = 0.6$ drag coefficients for clean and iced wing with WB33 artificial ice shapes having various levels of geometric fidelity from the F1 wind tunnel at $M = 0.09$ to 0.34.
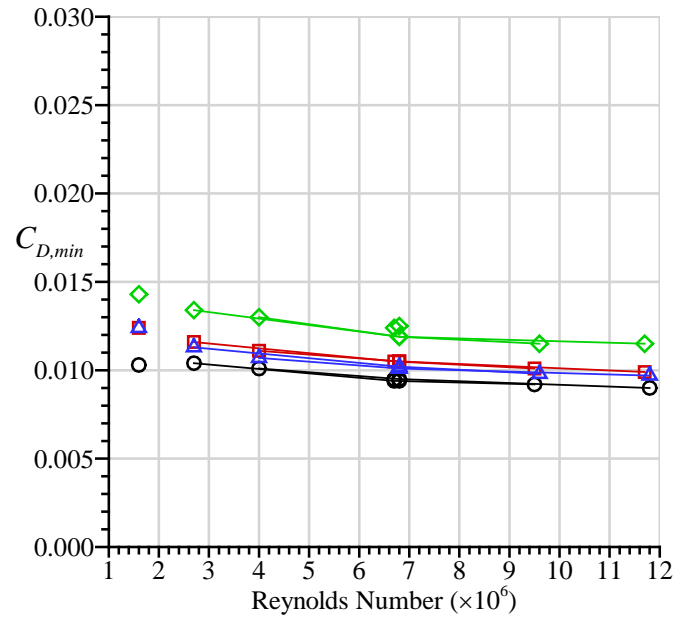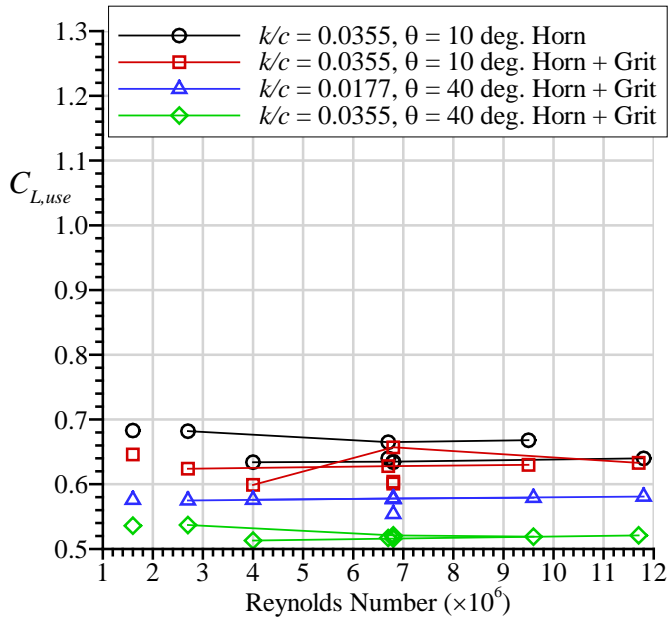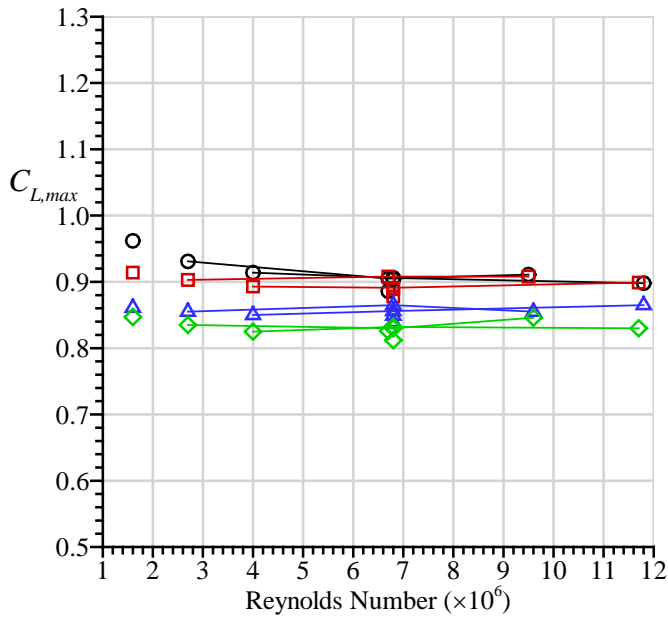
Page 13 of 19

10/19/2016

Figure 13. Effect of Reynolds number on maximum and usable lift coefficients for the iced wing with simple 3D horn ice shapes from the F1 wind tunnel at $M = 0.09$ to 0.34.

Figure 14. Effect of Reynolds number on minimum and $C_L = 0.6$ drag coefficients for the iced wing with simple 3D horn ice shapes from the F1 wind tunnel at $M = 0.09$ to 0.34.

D. Summary of Simple 3D Horn Ice Aerodynamic Effects

The results of the 13.3% scale model testing at the ONERA F1 wind tunnel were combined with the results of the 8.9% scale model testing at the WSU wind tunnel to develop a more complete understanding of simple 3D horn ice effects on swept wings. Due to the ever present limitations of testing time and resources, it was not possible to complete testing in one or both facilities on a full set of horn ice shapes: two horn heights ($k/c = 0.0177$ and 0.0355) and three horn angles ($\theta = 10$, 25 and 40 deg) with and without grit roughness. Therefore, these data must be combined in order to systematically

determine the effects of horn height, angle and roughness. Lee et al. [6,10] have written extensively on the comparison of aerodynamic data obtained in both facilities for equivalent clean and iced-wing configurations. Therefore, such detailed comparisons are beyond the scope of this paper. In general, the aerodynamic performance measured for equivalent iced-wing configurations matches very well between the F1 and WSU wind tunnels. However, specific values of the lift and drag-based performance parameters do not exactly agree. A main reason for this is that the Reynolds and Mach numbers cannot be exactly matched between the two facilities. Another reason had to do with accounting for the respective experimental absolute and bias uncertainties. In order to improve the interpretation of simple 3D horn ice effects for this paper, data for the $M = 0.09$ conditions from both F1 and WSU wind tunnels were not used. These data showed the most significant differences between each facility [6,10].

The results of this analysis are summarized in Fig. 15 for the lift-based performance parameters and in Fig. 16 for the drag-based performance parameters. It is readily apparent that there is quite a bit of variation in the data for each configuration. This variation is mostly due to the effects of Reynolds and Mach number that were discussed in the previous section. An additional factor is the combination of the F1 and WSU wind-tunnel data sets. In some ways, the "data spread" for each configuration may be thought of a practical type of uncertainty for iced wing results with simple 3D horn ice shapes. There would most certainly be much less "scatter" in the data if the results were limited to a single Reynolds and Mach number condition from one wind-tunnel facility. In spite of this variation, these results do yield some important findings.

Looking firstly at the behavior of $C_{L,max}$ in Fig. 15, the data for $\theta = 10$ deg horn angle show very little influence of horn height, with a larger difference for the $k/c = 0.0355$ horn in the smooth vs. rough configuration. This is contrasted with the behavior of $C_{L,use}$ for $\theta = 10$ deg horn angle where the horn height had a much larger impact. This effect can be seen in the pitching moment behavior previously shown in Fig. 10. The $C_{L,max}$ data for the $\theta = 25$ deg horn angle follow expected trends with the smaller, smooth horn ($k/c = 0.0177$) corresponding to the largest $C_{L,max}$ while the larger horn with grit roughness ($k/c = 0.0355$ + grit) corresponding to the lowest $C_{L,max}$. The same trend was not observed in the usable lift where the larger horn in a smooth configuration ($k/c = 0.0355$) yielded the lowest $C_{L,use}$ at $\theta = 25$ deg. The $C_{L,max}$ data for the $\theta = 40$ deg horn angle show a clear dependence upon the horn height for the rough configuration. A consistent result was observed for $C_{L,use}$. At the time of this writing, no data are available for the smooth configuration at $\theta = 40$ deg.

The performance effects for the drag-based parameters shown in Fig. 16 generally match the expected trends related to horn height for each horn angle. For example, at each horn angle of 10, 25 and 40 deg, the smaller and/or smooth horn had the lowest value of $C_{D,min}$ and $C_{D,0.6}$. At each horn angle there was a discernable increase in drag coefficient with the increase of horn height and/or the addition of grit roughness. However, the variation of $C_{D,min}$ for any given configuration was not linear with respect to horn angle. Instead, the maximum value of $C_{D,min}$ was measured for $\theta = 25$ deg. On the other hand, there was a nearly linear increase in $C_{D,0.6}$ with increasing horn angle. The effect of horn ice angle on $C_{D,min}$ for these configurations was likely mitigated by the corresponding negative wing angles of attack. In contrast, $C_{D,0.6}$ corresponded to much higher wing angles of attack, thereby significantly increasing the effect of horn ice angle as shown in Fig. 16.
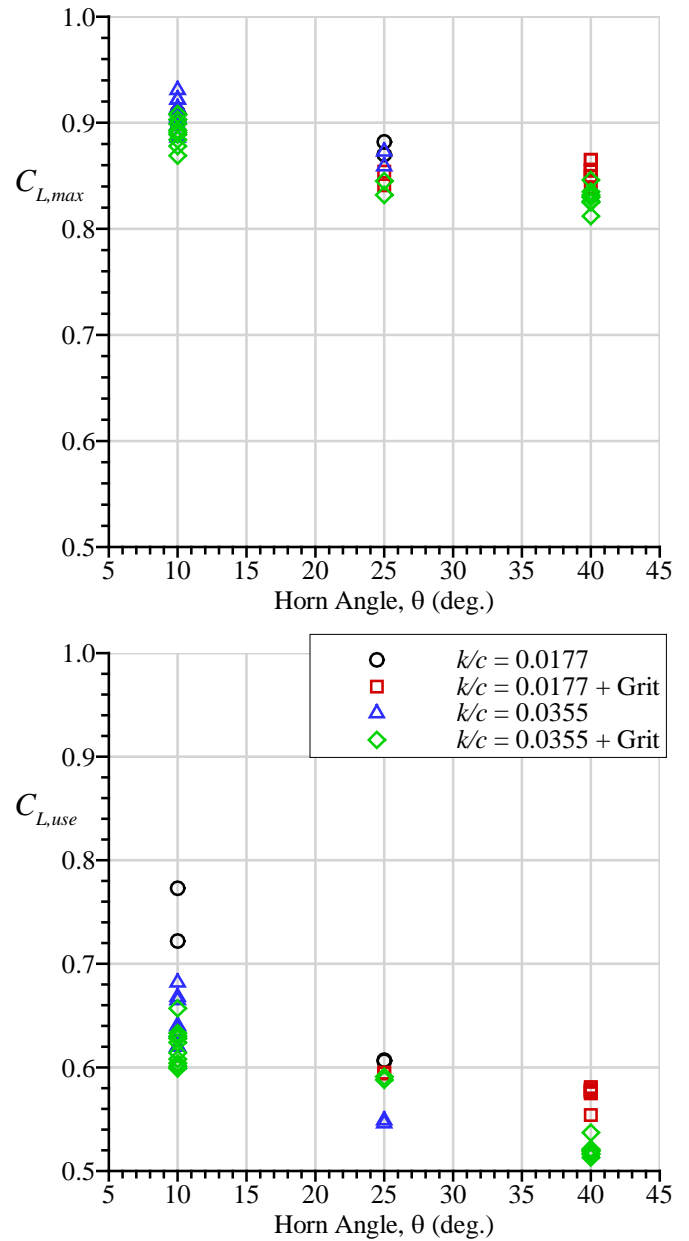
Figure 15. Effect of simple 3D horn ice shape height and angle maximum and usable lift coefficients. Data combined from F1 and WSU wind tunnels with $Re = 1.6 \times 10^6$ to 11.8×10^6 and $M = 0.17$ to 0.34.

The results presented in Fig. 15 for the dependence of $C_{L,max}$ on horn height and angle are generally consistent with the trends observed for similar experiments conducted on iced airfoils [26,29]. For example, the effect of horn height increases with increasing horn angle. Put another way, $C_{L,max}$ tends to be insensitive to horn height when located closer to the leading edge and thus having lower horn angles. As the horn angle increases, $C_{L,max}$ tends to become much more dependent upon horn height. The current data for the iced swept wing also includes an analysis of the usable lift coefficient that was not considered in previous iced airfoil studies. In terms of usable lift, the horn height did have a significant effect even for lower horn angles. This could be an important finding since usable lift may be more indicative of the impending iced-swept wing stall and need for additional pitch control than maximum lift coefficient. It should be noted, of course, that these findings are limited to a small set of

possible horn ice sizes and location in addition to being tested on a single swept-wing configuration. Clearly more data are needed in order to advance the universality of these results.
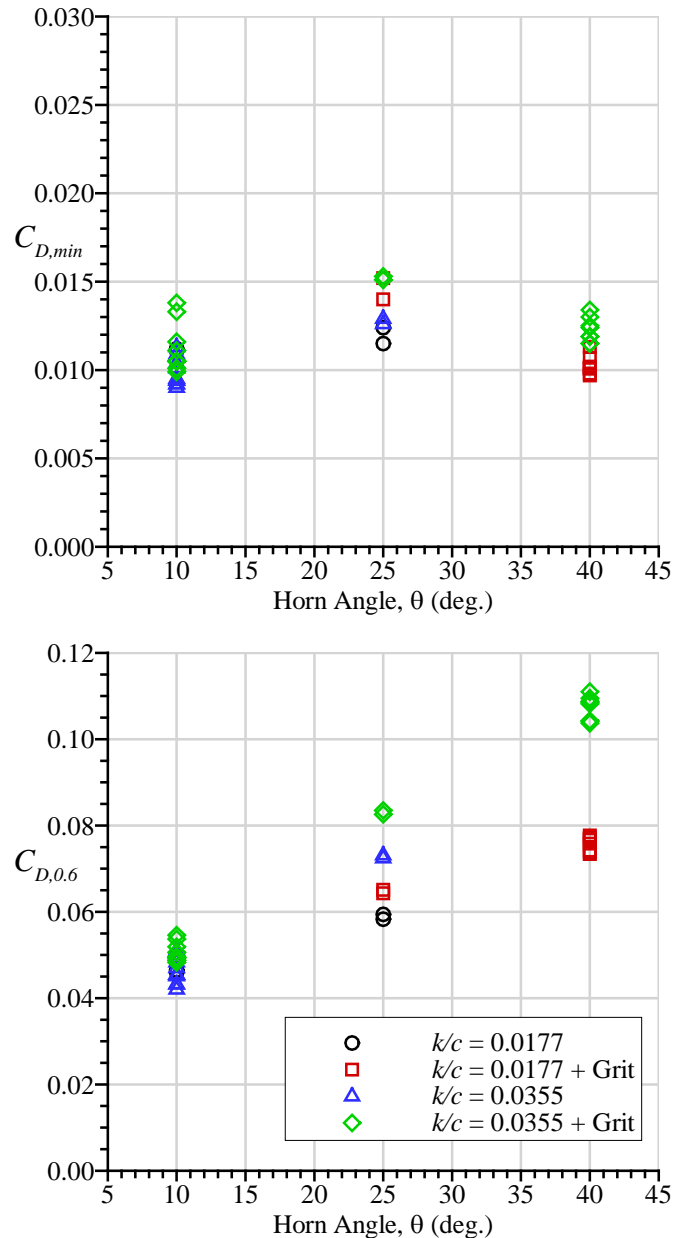

Figure 16. Effect of simple 3D horn ice shape height and angle on minimum and C_L = 0.6 drag coefficients. Data combined from F1 and WSU wind tunnels with Re = 1.6×10^6 to 11.8×10^6 and M = 0.17 to 0.34.

IV. Summary and Conclusion

This paper presents the results of aerodynamic testing of a swept wing with various leading-edge artificial ice shape configurations based upon a glaze icing condition. The objectives of this study were to determine the effect of the level of geometric fidelity required to reproduce the aerodynamics of a fully 3D, high-fidelity artificial ice shape including the effects of Reynolds and Mach number. Aerodynamic testing was conducted at the Wichita State University Beech wind tunnel and the ONERA F1 wind tunnel using 8.9% and

13.3% scale semispan wing models of the CRM65, respectively over a Reynolds number range of 0.8×10^6 to 11.8×10^6 and a Mach number range of 0.09 to 0.34. Force balance and surface pressure data were acquired. The high-fidelity artificial ice shape was based upon 3D scans of an App. C-based, glaze ice accretion in the NASA IRT and fabricated with rapid-prototype manufacturing. Additional artificial ice shapes were developed with decreasing geometric fidelity. One lower-fidelity artificial ice shape configuration was based upon a LEWICE3D simulation. The lowest-fidelity configurations were simple 3D horn ice geometries that represented only the maximum upper-surface ice thickness and horn location or angle with respect to the oncoming flow. The size and location of the simple 3D horn geometry was parametrically varied to understand the associated tradeoffs. In addition, the lower-fidelity artificial ice shapes were tested in a smooth condition and with added grit roughness that was sized according to the guidance provided in FAA Advisory Circular 25-25A.

The main conclusions regarding the aerodynamic effects were based upon analysis of four parameters defined in this (and previous) papers: maximum lift coefficient, usable lift coefficient, minimum drag coefficient and drag coefficient at a lift coefficient of 0.6. The usable lift coefficient was based upon an analysis of the wing pitching moment as indicative of stall progression on the wing. This parameter was developed because in many cases for the iced-wing configurations the stalling angle associated with maximum lift coefficient was higher than the clean wing stall angle. This represents a fundamental difference from past research on straight wings or airfoils with large, leading-edge artificial ice shapes where the stall angle was typically lower than the clean value.

When the lower-fidelity artificial ice shapes were tested in the smooth condition, they resulted in less conservative degradations to the clean wing lift and drag coefficients relative to the high-fidelity geometry that maintained all of the three-dimensional features of the original ice accretion. The 3D smooth and LEWICE3D artificial ice shapes resulted in similar aerodynamic performance despite the respective differences in the cross-section geometries. The addition of grit roughness to these geometries significantly improved the comparison in lift and pitching moment coefficients with the high-fidelity artificial ice-shape configuration. In the case of drag coefficient, there is some improvement in the comparison, but significant differences between the high-fidelity and lower-fidelity configurations remain. The effect of the baseline simple 3D horn ice artificial ice shape was also compared favorably in terms of lift and pitching moment to the 3D smooth and LEWICE3D configurations. The geometric differences in these configurations were made manifest in drag coefficient for low lift coefficient less than about 0.2.

The pressurization capability of the F1 wind-tunnel was used to investigate the effect of independent changes in Reynolds and Mach number on the clean and iced-wing configurations. In general, the aerodynamic performance data acquired on the wing with artificial ice shapes exhibited little variation with changes in Reynolds and Mach number over the range tested when compared against the clean-wing configuration. This variation was the least for the various WB33 artificial ice shapes such as the 3D high-fidelity, 3D smooth and LEWICE3D with grit roughness configurations. The aerodynamic data for the wing with the simple 3D horn ice configurations did exhibit slightly more variation with Reynolds and Mach number, but still significantly less than the clean configuration.

The results of the 13.3% scale model testing at the ONERA F1 wind tunnel were combined with the results of the 8.9% scale model testing at the WSU wind tunnel to develop a more complete understanding of simple 3D horn ice effects on swept wings. This aggregation of data resulted in quite a bit of variation of the lift and drag-based performance parameters for each horn-ice configuration. This variation was attributed to the effects of Reynolds and Mach number and the combination of the F1 and WSU wind-tunnel data sets. In spite of this variation, these results do yield some important findings. The data presented for the dependence of maximum lift coefficient on horn height and angle were generally consistent with the trends observed for similar experiments conducted on iced airfoils in past research. For example, the effect of horn height increases with increasing horn angle. Put another way, maximum lift coefficient tends to be insensitive to horn height when located closer to the leading edge and thus having lower horn angles. As the horn angle increases, maximum lift coefficient tends to become much more dependent upon horn height. The current data for the iced swept wing also includes an analysis of the usable lift coefficient that was not considered in previous iced airfoil studies. In terms of usable lift, the horn height did have a significant effect even for lower horn angles. This could be an important finding since usable lift may be more indicative of the impending iced-swept wing stall and need for additional pitch control than maximum lift coefficient. It should be noted that these findings are limited to a small set of possible horn ice sizes and location in addition to being tested on a single swept-wing configuration. Clearly more data are needed in order to advance the universality of these results.

References

1. Broeren, A.P., Potapczuk, M.G., Riley, J.T., Villiedieu, P., Moens, F., and Bragg, M.B., "Swept-Wing Ice Accretion Characterization and Aerodynamics," AIAA Paper 2013-2824, June 2013, also NASA/TM—2013-216555, Sept. 2013.
2. Broeren, A.P., Potapczuk, M.G., Lee, S., Malone, A.M., Paul, B.P., Jr., and Woodard, B.S., "Ice-Accretion Test Results for Three Large-Scale Swept-Wing Models in the NASA Icing Research Tunnel," AIAA Paper 2016-3733, June 2016; also NASA/TM—2016-219137, Sept. 2016.
3. Fujiwara, G.E.C., Bragg, M.B., Camello, S.C., and Lum, C., "Computational and Experimental Ice Accretions of Large Swept Wings in the Icing Research Tunnel," AIAA Paper 2016-3734, June 2016.
4. Radenac, E., "Validation of a 3D Ice Accretion Tool on Swept Wing of the SUNSET2 Program," AIAA Paper 2016-3735, June 2016.
5. Broeren, A.P., Lee, S., Woodard, B.S., Lum, C.W., and Smith, T.G., "Independent Effects of Reynolds and Mach Numbers on the Aerodynamics of an Iced Swept Wing," AIAA Paper 2018-3492, June 2018.
6. Lee, S., Broeren, A.P, Woodard, B.S., Lum, C.W., and Smith, T.S., "Comparison of Iced Aerodynamic Measurements on Swept Wing from Two Wind Tunnels," AIAA Paper 2018-3493, June 2018.
7. Woodard, B.S., Broeren, A.P., Lee, S., Lum, C.W., and Bragg, M.B., "Summary of Ice Shape Geometric Fidelity Studies on an Iced Swept Wing," AIAA Paper 2018-3494, June 2018.
8. Sandhu, N., Soltani, R., Bragg, M.B., Lum, C.W., Woodard, B.S., Broeren, A.P., and Lee, S., "Effect of Simulated Scalloped Ice on the Aerodynamics of a Swept-Wing at Low-Reynolds Number," AIAA Paper 2018-3495, June 2018.
9. Woodard, B.S., Broeren, A.P., Lee, S., and Bragg, M.B, "Experimental Aerodynamic Simulation of a Scallop Ice Accretion on a Swept Wing, International Conference on Icing of Aircraft, Engines and Structures, Minneapolis, MN, June 17-21, 2019 (submitted for publication).
10. Lee, S., Broeren, A.P Woodard, B.S., Lum, C.W., and Smith, T.S., "Comparison of Iced Aerodynamic Measurements on Swept Wing from Two Wind Tunnels, Part II," International Conference on Icing of Aircraft, Engines and Structures, Minneapolis, MN, June 17-21, 2019 (submitted for publication).
11. Soltani, M.R., Bragg, M.B., Yoshida, W.T., Woodard, B.S., and Lum, C.W., "Effects of a Low Fidelity Artificial Scallop Ice Shape on the Aerodynamics and Wake of a Swept-Wing," International Conference on Icing of Aircraft, Engines and Structures, Minneapolis, MN, June 17-21, 2019 (oral presentation).
12. Broeren, A.P., Addy, H.E., Jr., Bragg, M.B., Busch, G.T., Guffond, D., and Montreuil, E., "Aerodynamic Simulation of Ice Accretion on Airfoils," NASA/TP—2011-216929, June 2011.
13. Broeren, A.P Addy, H.E., Jr., Lee, S., and Monastero, M.C., "Validation of 3-D Ice Accretion Measurement Methodology for Experimental Aerodynamic Simulation," NASA/TM—2015-218724, July 2015.
14. Broeren, A.P, Addy, H.E., Jr., Lee, S., Monastero, M.C., and McClain, S.T., "Three-Dimensional Ice Accretion Measurement Methodology for Experimental Aerodynamic Simulation," *Journal of Aircraft*, Vol. 55, No. 2, Mar.-Apr. 2018, pp. 817-828.
15. Morgan, H.L., Ferris, J.C., McGhee, R.J., "A Study of High-Lift Airfoils at High Reynolds Numbers in the Langley Low-Turbulence Pressure Tunnel," NASA TM-89125, 1987.
16. Addy, H.E., Jr., and Chung, J.J., "A Wind Tunnel Study of Icing Effects on a Natural Laminar Flow Airfoil," AIAA Paper 2000-0095, Jan. 2000; also NASA/TM—2000-209775, Jan. 2000.
17. Addy, H.E., Jr., "Ice Accretions and Icing Effects for Modern Airfoils," NASA/TP-2000-210031, April 2000; also U.S. Dept. of Transportation/Federal Aviation Administration Rept. DOT/FAA AR-99/89, April 2000.
18. Addy, H.E., Jr., Broeren, A.P., Zoeckler, J.G., and Lee, S., "A Wind Tunnel Study of Icing Effects on a Business Jet Airfoil," AIAA Paper 2003-0727, Jan. 2003; also NASA/TM—2003-212124, Feb. 2003.
19. Bragg, M.B., Broeren, A.P., and Blumenthal, L.A., "Iced-Airfoil Aerodynamics," *Progress in Aerospace Sciences*, Vol. 41, No. 5, July 2005, pp. 323-418.
20. Broeren, A.P., Bragg, M.B., and Addy, H.E., Jr., "Effect of Intercycle Ice Accretions on Aerodynamic Performance," *Journal of Aircraft*, Vol. 41, No. 1, Jan.-Feb. 2004, pp 165-174.
21. Broeren, A.P., Bragg, M.B., Addy, H.E., Jr., Lee, S., Moens, F., and Guffond, D., "Effect of High-Fidelity Ice Accretion Simulations on the Performance of a Full-Scale Airfoil Model," *Journal of Aircraft*, Vol. 47, No. 1, Jan.-Feb. 2010, pp. 240-254; also NASA/TM-2010-216344, Jun. 2010.
22. Busch, G.T., Broeren, A.P., and Bragg, M.B., "Aerodynamic Simulation of a Horn-Ice Accretion on a Subscale Model," *Journal of Aircraft*, Vol. 45, No. 2, Mar.-Apr. 2008, pp. 604-613.
23. Busch, G.T., Broeren, A.P., and Bragg, M.B., "Aerodynamic Fidelity of Sub-scale Two-Dimensional Ice Accretion Simulations," AIAA Paper 2008-7062, Aug. 2008.
24. Busch, G.T., and Bragg, M.B., "Experimental Study of Full-Scale Iced-Airfoil Aerodynamic Performance using Sub-scale Simulations," AIAA Paper 2009-4264.

10/19/2016

25. Papadakis, M., Glie-Laflin, B.E., Yousef, G.M., and Ratvasky, T.P., "Aerodynamic Scaling Experiments with Simulated Ice Accretions," AIAA Paper 2001-0833, Jan. 2001.

26. Kim, H.S., and Bragg, M.B., "Effects of Leading-Edge Ice Accretion Geometry on Airfoil Aerodynamics," AIAA Paper 99-3150, June 1999.

27. Papadakis, M., Alansatan, S., and Seltmann, M., "Experimental Study of Simulated Ice Shapes on a NACA 0011 Airfoil," AIAA Paper 99-0096, Jan. 1999.

28. Papadakis, M., Alansatan, S., and Wong, S.-C., "Aerodynamic Characteristics of a Symmetric NACA Section with Simulated Ice Shapes," AIAA Paper 2000-0098, Jan. 2000.

29. Broeren, A.P., Lee, S., LaMarre, C.M., and Bragg, M.B., "Effect of Airfoil Geometry on Performance with Simulated Ice Accretions Vol. 1: Experimental Investigation." DOT/FAA/AR-03/64, Aug. 2003.

30. Lee, S., and Bragg, M.B., "Investigation of Factors Affecting Iced-Airfoil Aerodynamics," *Journal of Aircraft*, Vol. 40, No. 3, May-June 2003, pp. 499-508.

31. Vassberg, J.C., DeHann, M.A., Rivers, S.M., and Wahls, R.A., "Development of a Common Research Model for Applied CFD Validation Studies," AIAA Paper 2008-6919, Aug. 2008.

32. Rivers, M.B., and Dittberner, A., "Experimental Investigation of the NASA Common Research Model," AIAA Paper 2010-4218, June 2010.

33. Rivers, M.B., and Dittberner, A., "Experimental Investigations of the NASA Common Research Model in the NASA Langley National Transonic Facility and the NASA Ames 11-Ft Transonic Wind Tunnel," AIAA Paper 2011-1126, Jan. 2011.

34. Vassberg, J. C., Tinoco, E. N., Mani, M., Rider, B., Zickuhr, T., Levy, D.W., Brodersen, O., Eisfeld, B., Crippa, S., Wahls, R. A., Morrison, J. H., Mavriplis, D.J., and Murayama, M., "Summary of the Fourth AIAA CFD Drag Prediction Workshop," AIAA Paper 2010-4547, June 2010.

35. Torz-Dupuis, L., "Test NASA SUNSET II of the CRM65 Wing Model Representative of the CRM65 Wing at 1/7.5 on Half Model Set-up in the ONERA F1 Wind Tunnel," ONERA Report No. PV 4/23611 DMPE/DSFM, Dec. 2017.

36. Coleman, H.W., and Steele, W.G., *Experimentation and Uncertainty Analysis for Engineers*, Wiley-Interscience, New York, 1989, pp.40-118.

37. Kline, S., and McClintock, F.A, "Describing Uncertainties in Single Sample Experiments," *Mechanical Engineering*, Vol. 75, No. 1, 1953, pp. 3-8.

38. Broeren, A.P., Woodard, B.S., Diebold, J.M., and Moens, F., "Low-Reynolds Number Aerodynamics of an 8.9 Percent Scale Semispan Swept Wing for Assessment of Icing Effects," AIAA Paper 2017-4372, June 2017, also NASA/TM—2017-219533, July 2017.

39. Camello, S.C., Bragg, M.B., Broeren, A.P., Lum, C.W., Woodard, B.S., and Lee, S., "Effect of Ice-Shape Fidelity on Swept-Wing Aerodynamic Performance," AIAA Paper 2017-4373, June 2017.

40. Woodard, B.S., Broeren, A.P., Diebold, J.M., and Bragg, M.B., "Preliminary Testing of Low Reynolds Number Aerodynamics for a Swept Wing with Artificial Ice Roughness," FAA Technical Report, DOT/FAA/TC-17/48, Sept. 2017.

41. Barlow, J.B., Rae, W.H., Jr., Pope, A., *Low-Speed Wind Tunnel Testing*, John Wiley & Sons, Inc., 3rd Ed., 1999, pp. 367-425.

42. "Data Reduction System: Boundary Corrections Three Dimensional Aircraft," Walter H. Beech Wind Tunnel Engineering Process Description, April 2014.

43. Camello, S.C., Lee, S., Lum, C.W., and Bragg, M.B., "Generation of Fullspan Leading-Edge 3D Ice Shapes for Swept-Wing Aerodynamic Testing," AIAA Paper 2016-3737, June 2016.

44. Yadlin, Y., Monnig, J.T., Malone, A.M., and Paul, B.P., "Icing Simulation Research Supporting the Ice-Accretion Testing of Large-Scale Swept Wing Models," NASA/CR—2018-2197891, Mar. 2018, Also DOT/FAA/TC-18/17.

45. Furlong, G.C., and McHugh, J.G., "A Summary and Analysis of the Low-speed Longitudinal Characteristics of Swept Wings at High Reynolds Number, NACA-TR-1339, Jan. 1957.

46. Lynch, F.T., and Khodadoust, A., "Effects of Ice Accretions on Aircraft Aerodynamics," *Progress in Aerospace Sciences*, Vol. 37, No. 8, Nov. 2001, pp. 669-767.

Contact Information

For questions regarding the manuscript, please contact Andy Broeren (abroeren@nasa.gov).

Acknowledgments

Definitions/Abbreviations

b	wing span
c	local chord length perpendicular to the leading edge
C_D	drag coefficient
$C_{D,min}$	minimum drag coefficient
$C_{D,0.6}$	drag coefficient at $C_L = 0.6$
C_L	lift coefficient
$C_{L,max}$	maximum lift coefficient

10/19/2016

$C_{L,use}$	usable lift coefficient	Re	freestream Reynolds number based on mean aerodynamic chord
C_M	quarter-chord mean aerodynamic chord pitching moment coefficient	$V_{s,1g}$	aircraft 1-g stall speed
$C_{M,min}$	minimum quarter-chord mean aerodynamic chord pitching moment coefficient	x	wing streamwise coordinate
		y	wing spanwise coordinate
C_p	model surface pressure coefficient	z	wing thickness coordinate
k	ice horn height	α	model angle of attack
LWC	icing cloud liquid water content	α_{stall}	stalling angle of attack, consistent with the maximum lift coefficient
M	freestream Mach number	α_{use}	usable angle of attack, consistent with the usable lift coefficient
MAC	mean aerodynamic chord		
MCCS	maximum combined cross section	θ	ice horn angle
MVD	median volumetric diameter of icing cloud drop distribution		
p_o	freestream total pressure		
q_∞	freestream dynamic pressure		

10/19/2016